

# Solar Backscatter Ultraviolet (BUV) Retrievals

## of Mid-Stratospheric Aerosols from the 2022 Hunga Eruption

Robert J. D. Spurr<sup>1</sup>, Matt Christi<sup>2</sup>, Nickolay A. Krotkov<sup>3</sup>, Won-Ei Choi<sup>4</sup>, Simon Carn<sup>5</sup>, Can Li<sup>3</sup>, Natalya Kramarova<sup>3</sup>, David Haffner<sup>6</sup>, Eun-Su Yang<sup>7,3</sup>, Nick Gorkavyi<sup>8,3</sup>, Alexander Vasilkov<sup>9,3</sup>, Krzysztof Wargan<sup>8,3</sup>, Omar Torres<sup>3</sup>, Diego Loyola<sup>10</sup>, Serena Di Pede<sup>11</sup>, J. Pepijn Veefkind<sup>11,12</sup>, Parker Case<sup>13</sup>, Thomas Schroeder<sup>14</sup>, and Pawan K. Bhartia<sup>15</sup>

<sup>1</sup> RT Solutions, Inc., Cambridge, MA 02138, USA

<sup>2</sup> Independent Researcher, Fort Collins, CO 80524, USA

<sup>3</sup> NASA Goddard Space Flight Center, Greenbelt, MD 20771, USA

<sup>4</sup> NASA Postdoctoral Program, Oak Ridge Associated Universities, Oak Ridge, TN 37830, USA

<sup>5</sup> Michigan Technological University, Houghton, MI 49931, USA

<sup>6</sup> Independent Researcher, Glen Ellen, CA 95442, USA

<sup>7</sup> Science and Technology Corporation, VA 23666, USA

<sup>8</sup> Science Systems and Applications, Inc., Lanham, MD 20706, USA

<sup>9</sup> ADNET Systems, Inc., Lanham, MD 20706, USA

<sup>10</sup> German Aerospace Centre (DLR), Oberpfaffenhofen, 82234 Wessling, Germany

<sup>11</sup> Royal Netherlands Meteorological Institute (KNMI), 3730 AE De Bilt, The Netherlands

<sup>12</sup> Delft University of Technology, 2628 CN Delft, The Netherlands

<sup>13</sup> Earth System Science Interdisciplinary Center (ESSIC), University of Maryland, College Park, MD 20740, USA

<sup>14</sup> Commonwealth Scientific and Industrial Research Organization (CSIRO) Environment, Brisbane, QLD 4001, Australia

<sup>15</sup> Goddard Earth Sciences Technology and Research (GESTAR) II, University of Maryland Baltimore County, Baltimore, MD 21228, USA

*Correspondence to:* Nickolay A. Krotkov (Nickolay.a.krotkov@nasa.gov)

**Abstract.** On January 15, 2022, a highly explosive eruption of the submarine Hunga volcano (Kingdom of Tonga) generated the largest stratospheric hydration event ever observed and the largest aerosol perturbation since the 1991 Pinatubo eruption. Here, we develop a novel method for satellite retrieval of stratospheric aerosol optical depth (AOD) and layer peak height ( $Z_p$ ) using solar backscattered ultraviolet (BUV) radiation; this is made possible by the exceptional mid-stratospheric altitude of the Hunga aerosols. We analyze BUV observations of the Hunga stratospheric aerosol cloud on January 17, 2022 (47 hours after the eruption), using BUV band 1 measurements from the Tropospheric Monitoring Instrument (TROPOMI) on board the ESA/Copernicus Sentinel-5 precursor (S5P) satellite, and the Ozone Mapping and Profiling Suite- Nadir Profiler (OMPS-NP) on board the National Oceanic and Atmospheric Administration (NOAA)-20 satellite. We retrieve AOD and  $Z_p$  by fitting hyperspectral BUV radiance ratios in a narrow spectral window restricted to 289–296 nm, chosen in order to reduce interference from tropospheric clouds while highly sensitive to stratospheric aerosols located above ozone maximum altitude.

38 The retrieval employs radiative transfer calculations from the Vector Linearized Discrete Ordinate Radiative Transfer  
39 (VLIDORT) forward model. We assume a single Hunga aerosol layer composed of polydisperse sulfuric acid spherical  
40 particles embedded in a Rayleigh atmosphere with a known ozone profile. The ozone profile is supplied from a version of the  
41 MERRA-2 Stratospheric Composition Reanalysis of the Microwave Limb Sounder (MLS) on board NASA Earth Observing  
42 System-chemistry (EOS Aura) satellite — produced by NASA's Global Modeling and Assimilation Office using a stratospheric  
43 chemistry model and MERRA-2 meteorology. We also include a dynamic SO<sub>2</sub> layer, which coincides spatially with the  
44 retrieved aerosol vertical profile, and with the total loading normalized to the stratospheric SO<sub>2</sub> vertical column density from  
45 the operational TROPOMI SO<sub>2</sub> product. We validate our AOD retrievals against ground-based AERONET direct-sun AOD  
46 measurements as well as co-located OMPS-NP retrievals, and  $Z_p$  retrievals against Cloud-Aerosol Lidar with Orthogonal  
47 Polarization (CALIOP) overpasses using Lagrangian trajectory modeling. We estimate the total Hunga stratospheric wet  
48 aerosol mass (sulfuric acid solution droplets, including water uptake) to be  $M_{aer} \sim 0.5 \pm 0.05 \text{ Tg}$ . This value is consistent with  
49 our previous BUV estimates of Hunga sulfur dioxide (SO<sub>2</sub>) emissions ( $\sim 0.4\text{--}0.5 \text{ Tg SO}_2$ ) and rapid conversion of SO<sub>2</sub> to sulfate  
50 aerosol. Based on these BUV retrievals we can also estimate the sulfuric acid (H<sub>2</sub>SO<sub>4</sub>) mass fraction  $w \sim 0.4$  and H<sub>2</sub>SO<sub>4</sub>/H<sub>2</sub>O  
51 solution density:  $\rho \sim 1.34 \text{ g/cm}^3$ . These new values represent an extreme departure from the stratospheric background sulfate  
52 aerosol (Junge layer), which is typified by values of  $w \sim 0.75$  and  $\rho \sim 1.7 \text{ g/cm}^3$  supported by decades of observations of the  
53 lower stratosphere during both quiescent and volcanically impacted periods. The new low values, inferred from BUV  
54 observations and backed up by microphysical modeling, are a result of the uniquely water-rich conditions in the early Hunga  
55 plume. Relative humidity in the plume, as modeled by the NASA Goddard Earth Observing System Chemistry-Climate Model  
56 with the Community Aerosol and Radiation Model for Atmospheres (CARMA), reached values as high as 60%, compared to  
57 background values closer to 1%. These findings are unique in the long-term observational record of the stratosphere; similar  
58 relative humidities only otherwise occur in overshooting clouds or cold winter hemisphere vortices.

## 59 **1 Introduction**

60 A paroxysmal eruption of the submarine Hunga volcano (Kingdom of Tonga; 20.550°S, 175.385°W) at ~04:15 UTC on  
61 January 15, 2022 produced a steam-driven eruption column up to ~58 km altitude (Carr et al., 2022; Millán *et al.*, 2022) and  
62 injected a massive plume of water vapor (H<sub>2</sub>O), sulfur dioxide (SO<sub>2</sub>), and aerosols directly into the Southern tropical  
63 stratosphere (Carn et al., 2022; Coy et al., 2022; Khaykin et al., 2022; Millán et al., 2022; Legras et al., 2022; Schoeberl et al.,  
64 2023; Sellitto et al., 2022; Taha et al., 2022; Vömel et al., 2022). This was the largest volcanic explosion since Pinatubo in  
65 1991, with a designated Volcanic Explosivity Index (VEI) of 5–6. The Hunga eruption produced enormous umbrella cloud(s)  
66 with diameter(s) >500 km, global Lamb waves (Kubota et al., 2022; Matoza et al., 2022), regional volcanic ash fall (Kelly et  
67 al., 2024), and Pacific-wide tsunamis (Lynett et al., 2022; Shrivastava et al., 2023).

68

69 Although volcanic ash ejecta remained at relatively low altitudes and quickly fell out over the Tonga area (Kelly et al., 2024),  
70 sub-micron non-absorbing, non-depolarizing sulfate-type aerosol particles persisted in the mid-stratosphere (Khaykin et al.,  
71 2022; Sellitto et al., 2022; Taha et al., 2022; Baron et al., 2023; Bernath et al., 2023; Bian et al., 2023; Boichu et al., 2023;  
72 Bourassa et al., 2023; Duchamp et al., 2023; Manney et al., 2023; Kahn et al., 2024; Stocker et al., 2024; Sicard et al., 2025).  
73 Discussions on the H<sub>2</sub>O-accelerated conversion of volcanic SO<sub>2</sub> to sulfate aerosol may be found in previous studies (Carn et  
74 al., 2022; Legras et al., 2022; Sellitto et al., 2022; Zhu et al., 2022; Asher et al., 2023, Boichu et al., 2023; Bruckert et al.,  
75 2025; Sadeghi et al., 2025; Stenchikov et al., 2025).

76  
77 Initial estimates of the Hunga SO<sub>2</sub> emissions from solar backscatter ultraviolet (BUV) near-nadir satellite measurements did  
78 not account for interference from stratospheric aerosols; indeed, unexpectedly low amounts were reported for an eruption of  
79 this magnitude: ~0.4–0.5 Tg SO<sub>2</sub> (Carn et al., 2022). Infrared (IR) satellite measurements from the Cross-track Infrared Sounder  
80 (CrIS) instrument (Hyman and Pavolonis, 2020) retrieved a similar amount: ~0.4 Tg SO<sub>2</sub> (Sadeghi et al., 2025); however,  
81 retrievals from the Infrared Atmospheric Sounding Interferometer (IASI) reported roughly double this amount, i.e., >1 Tg SO<sub>2</sub>  
82 (Sellitto et al., 2022, 2024; Bruckert et al., 2025). These conflicting estimates provide a strong motivation to re-analyze BUV  
83 SO<sub>2</sub> measurements with explicit consideration of Hunga aerosol interference. To do this, we need first to introduce a suitable  
84 Hunga aerosol optical model in the UV and then develop a new quantitative BUV retrieval of non-absorbing stratospheric  
85 aerosol particles. Such nadir-BUV aerosol retrievals were not thought to be possible prior to the Hunga event; indeed, this is  
86 the first eruption in the modern satellite era to inject particles directly into the mid-stratosphere above the tropical ozone (O<sub>3</sub>)  
87 density peak at ~25 km (Carr et al., 2022; Taha et al., 2022). This unique geophysical event provides access to solar  
88 backscattered shortwave UV radiation (< 300 nm wavelength) that is absorbed by ozone before reaching the lower altitudes  
89 typical of volcanic aerosol injections. Another motivation for the present study is that during the early dispersion phase, the  
90 presence of Hunga aerosols significantly affected the BUV satellite retrievals of stratospheric ozone (Bhartia et al., 1993;  
91 Torres and Bhartia, 1995; Kramarova et al., 2024), as well as ocean color retrievals (Franz et al., 2024).

92  
93 Figure 1 shows a Visible Infrared Imaging Radiometer Suite (VIIRS) true color map from January 17, 2022, two days after  
94 the main Hunga eruption. The approximate locations of two distinct Hunga plumes are outlined over the Queensland region  
95 of Australia (Aerosol-rich plume; C1) and over the Coral Sea (SO<sub>2</sub>-rich plume; C2) – see Fig. 5d in Carn et al. (2022) and  
96 Figs. 4b–d in Legras et al. (2022). These two plumes showed different altitudes and compositions and evolved differently  
97 during the first weeks after the eruption before eventually mixing. The aerosol-rich C1 plume was also water-rich, which likely  
98 accelerated the SO<sub>2</sub>-to-sulfate conversion and enhanced radiative cooling, thus contributing to its more rapid descent compared  
99 to that of the SO<sub>2</sub>-rich C2 plume. Also indicated in Fig. 1 are the overpass times of key satellite tracks: the National Oceanic  
100 and Atmospheric Administration (NOAA)-20 Ozone Mapping and Profiler Suite (OMPS) Nadir Profiler (NP) swath (~4:00–  
101 4:09 UTC), the Cloud-Aerosol Lidar with Orthogonal Polarization (CALIOP) daytime track (~5:23–5:34 UTC), and nighttime  
102 tracks (~16:14–16:25 UTC and ~17:54–18:05 UTC). These times indicate that the observations were not simultaneous, but

103 together they provide a complementary view of the rapidly evolving plume ( $\approx 20^\circ$  longitude per day; see also Fig. 7). The  
 104 OMPS nadir profiler sensor (OMPS-NP), which has a spatial resolution of 50 km at nadir, is designed to measure stratospheric  
 105 ozone profiles using BUV wavelengths above and below 300 nm, but as a nadir-sounding sensor it does not provide adequate  
 106 horizontal coverage of the Hunga aerosol plume. Nevertheless, the well-placed OMPS-NP overpass of the Hunga plume on  
 107 January 17 (Fig. 1) did provide the first spectral observations of significantly enhanced BUV radiances produced by the Hunga  
 108 aerosols at wavelengths around 300 nm.

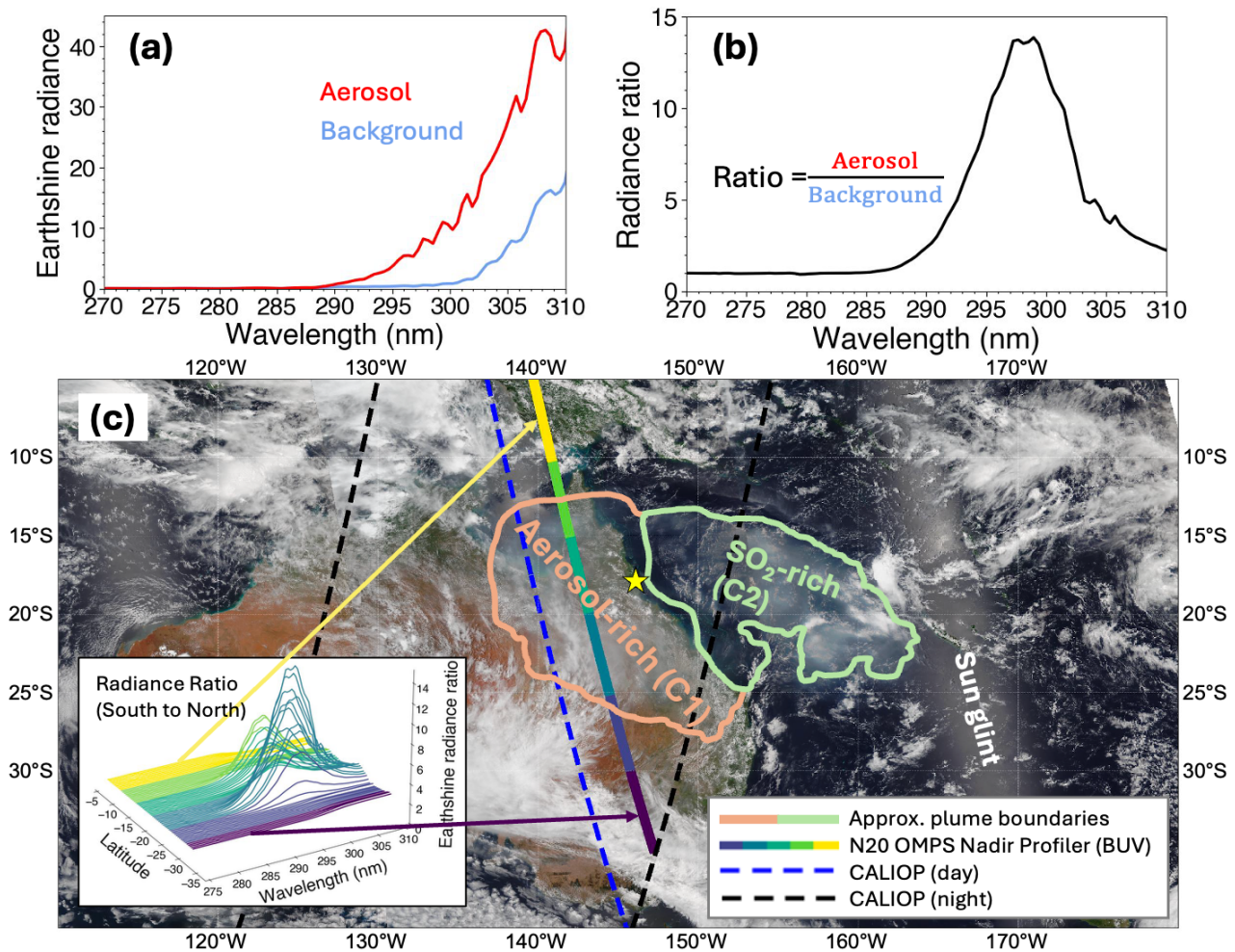


**Figure 1:** (a) Shortwave BUV radiances (270–310 nm) of aerosol-rich and background (aerosol-free) regions. (b) Spectral radiance ratios (aerosol/background). (c) True-color NOAA-20 VIIRS map of Australia and the Coral Sea on January 17, 2022. The solid line with colored segments shows the suborbital track of the NOAA-20 OMPS-NP (~4:00–4:09 UTC). The inset panel at bottom left shows the variation of spectral radiance ratio with latitude measured by OMPS-NP in the Hunga aerosol plume. Dashed lines are CALIOP ground tracks—blue for daytime (~5:21–5:32 UTC) and black for nighttime (left: ~17:54–18:05 UTC, right: ~16:14–16:25 UTC). The yellow star indicates the location of the Aerosol Robotic Network (AERONET) Lucinda site (18.5198°S; 146.3861°E; elevation: 8.0 m).

109

110 Accordingly, to estimate total Hunga aerosol optical depth (AOD), layer peak height ( $Z_p$ ), and column mass, we have analyzed  
111 BUV observations taken by an imaging spectrometer — TROPospheric Monitoring Instrument (TROPOMI) on board the  
112 Copernicus Sentinel-5 precursor (S5P) satellite. TROPOMI is eminently suitable for this task, because of its contiguous daily  
113 coverage and high spatial resolution (nominally 5.5 km by 28 km below 300 nm in band 1) (Veefkind et al., 2012; Ludewig et  
114 al., 2020). On January 17 at ~03:16 UTC (47 hours after the January 15 eruption) the bulk of the Hunga aerosol was observed  
115 over Northeast Australia (Fig. 1), while the bulk of the attendant SO<sub>2</sub> plume was trailing over the Coral Sea (see also Fig. 5d  
116 of Carn et al., 2022).

117 We use such BUV spectral enhancements to develop a new algorithm for retrievals of non-absorbing aerosol optical depth  
118 (AOD) and peak-height ( $Z_p$ ) and estimates of column wet aerosol mass (*i.e.*, sulfuric acid solution droplets, H<sub>2</sub>SO<sub>4</sub>/H<sub>2</sub>O  
119 including water uptake),  $m_{aer}$ . The retrieval algorithm is based on spectral fitting of hyperspectral BUV radiance ratios with  
120 the forward model driven by the Vector Linearized Discrete Ordinate Radiative Transfer (VLIDORT) model (Spurr and Christi  
121 2019) and combined with polydisperse Mie calculations of aerosol optical properties (*i.e.*, spectral extinction and scattering  
122 matrices). Based on collocated Cloud-Aerosol Lidar with Orthogonal Polarization (CALIOP) backscatter measurements (Fig.  
123 1), we have assumed a single aerosol layer composed of spherical polydisperse homogeneous sulfuric acid in water solution  
124 H<sub>2</sub>SO<sub>4</sub>/H<sub>2</sub>O particles embedded in a Rayleigh-scattering atmosphere with a known ozone and temperature profiles. We also  
125 included a dynamic SO<sub>2</sub> vertical profile, assumed spatially coincident with the retrieved aerosol plume, but normalized to the  
126 TROPOMI operational stratospheric SO<sub>2</sub> column density (Theys et al., 2017).

127

128 This paper begins by summarizing the TROPOMI UV band 1 (UV1) measurements (Section 2). Section 3 describes our  
129 retrieval algorithm, comprising an overview of the retrieval strategy (Section 3.1), deployment of the VLIDORT-based forward  
130 model component (3.2), the inverse model (3.3), a discussion on aerosol optical properties and trace gas parameterization (3.4),  
131 and a validation of the retrieval algorithm using synthetic data. In Section 4, we present our results on the retrieval and  
132 validation of aerosol peak height (Section 4.1) and AOD (Section 4.2), followed by estimates of the column wet aerosol mas,  
133  $m_{aer}$  and total aerosol mass including water uptake,  $M_{aer}$  (Section 4.3). In addition, we estimate H<sub>2</sub>SO<sub>4</sub> (sulfate) mass fraction,  
134  $w$  and H<sub>2</sub>SO<sub>4</sub>/H<sub>2</sub>O particle mass density,  $\rho$  (Section 4.4). Section 4.5 contains comparisons with recent IR-based retrievals of  
135 SO<sub>2</sub> and Hunga aerosol mass from other studies of this unique event. Section 5 concludes with a summary of the paper along  
136 with final remarks.

## 137 2. Solar Backscatter Measurements in the UV (BUV)

138 This section is concerned with measurement data. First, we focus on the TROPOMI band 1 backscatter measurements used  
139 for the aerosol plume retrieval; this is followed by a discussion on anomalies in the satellite ozone record caused by the Hunga  
140 eruption.

## 141 2.1 TROPOMI Band 1 radiances and radiance ratios

142 A detailed description of the current version of the TROPOMI Level 1B radiance product (L1B\_RA\_BD1), including the data  
143 file format in NETCDF-4 and the data fields, is given in the TROPOMI Level 1B product “readme” file  
144 (<https://doi.org/10.5270/S5P-kb39wni>, Ludewig et al., 2023). TROPOMI provides excellent spatial resolution and daily global  
145 coverage in the shortwave BUUV band 1 (267–300 nm); however, TROPOMI has known radiometric and sensor degradation  
146 issues in band 1 (Ludewig et al., 2020), and it has proved necessary to apply soft calibration techniques to improve the data  
147 quality. The TROPOMI soft calibration is computed from characterization of the differences between measured and modelled  
148 radiances (absolute residuals), following a similar approach to that described in Mettig et al. (2021). Since this soft calibration  
149 is designed to correct input radiances for the TROPOMI ozone profile data product, forward Radiative Transfer (RT) model  
150 calculations were performed over the combined spectral range of band 1 and 2 (270–330 nm). Pressure, temperature, and ozone  
151 profiles from the Copernicus Atmospheric Monitoring Service (CAMS) were used as inputs to the RT model. Additionally,  
152 CAMS ozone profiles were scaled to match total ozone columns derived from the independent OMPS Nadir Mapper gridded  
153 column ozone data (Jaross 2017). The modelled atmosphere does not contain clouds or aerosols, but particulate scattering  
154 effects are compensated through adjustment of the surface albedo. With this in mind, we have fitted the scene albedo in a small  
155 spectral window (328–330nm) and assumed this albedo to be representative for the entire fitting window. Radiance residuals  
156 (measurement to model) are computed for single seasonal TROPOMI orbits over the Pacific Ocean. To compute correction  
157 parameters, the radiance residuals are compiled separately for each year and then applied to the radiance measurement in that  
158 year. Correction parameters are provided as a function of the TROPOMI across-track position (i.e., CCD detector row),  
159 wavelength and radiance level; they are applied to the uncorrected radiance signal ( $R_{\text{uncorr}}$ ) by subtracting the bias ( $R_{\text{corr}} =$   
160  $R_{\text{uncorr}} - \text{bias}$ ). For TROPOMI orbits 22086 and 22087 affected by Hunga aerosols we apply the fixed correction available for  
161 the highest radiance.

162 One option for constructing the retrieval measurement vector is to use sun-normalized radiances, or the “N-values” (defined  
163 as  $N(\lambda) = -100 \log_{10} \left( \frac{I(\lambda)}{F(\lambda)} \right)$  where  $I$  denotes Earthshine radiance and  $F$  solar irradiance), as shown in Fig. 2 for two  
164 TROPOMI orbits overpassing Hunga aerosol plume on January 17, 2022 (eastern orbit 22086 and the following orbit 22087)  
165 at four wavelengths, representative of the selected spectral fitting window:  $\lambda = 287.9\text{nm}, 292.5\text{nm}, 295.1\text{nm}, 297.9\text{nm}$ .

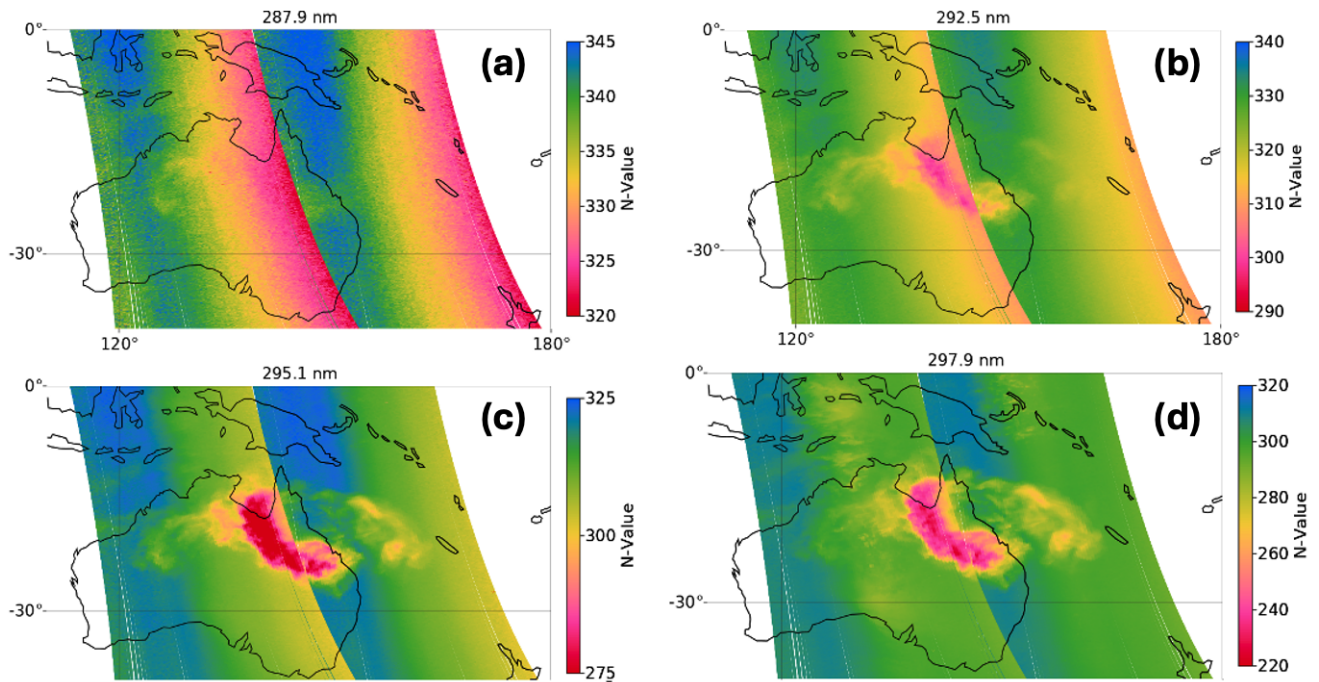


**Figure 2: Maps of the Hunga aerosol plume on January 17, 2022, using TROPOMI UV1 sun-normalized radiances before applying soft-calibration at four wavelengths at (a) 287.9, (b) 292.5, (c) 295.1, and (d) 297.9 nm in orbits 22086 (right-hand swath) and 22087 (left-hand swath). Plotted are the N-values, defined as  $N(\lambda) = -100 \log_{10} \left( \frac{I(\lambda)}{F(\lambda)} \right)$ , where  $I(\lambda)$  denotes Earthshine radiance, and  $F(\lambda)$  the solar irradiance. Note the different N-value scales for different wavelengths.**

166

167 However, in order to emphasize the Hunga aerosol spectral signal and to reduce its dependence on TROPOMI band 1  
 168 calibration and degradation issues, we prefer to use BUV *radiance ratios*, in which the radiance values from the orbit 22086  
 169 and 22087 pixels are normalized to background radiances for the same cross-track pixels from an adjacent aerosol-free orbit,  
 170 in this case TROPOMI orbit 22085. Radiance ratios are plotted in Fig.3. The advantage of normalizing to background radiances  
 171 is that this pixel-wise division leads to a partial cancellation of known radiometric and degradation interferences from the  
 172 TROPOMI band 1, as reported in Ludewig et al. (2020). We do account for the ozone profile differences between the orbits  
 173 using MERRA-2 Stratospheric Composition Reanalysis of the Microwave Limb Sounder (MLS) on board NASA EOS Aura  
 174 satellite as described later in section 2.2. The normalization requires correction for tropospheric clouds if one uses longer band  
 175 2 wavelengths (see example for background pixel 1 in Fig. 3). Therefore, in this study we only use a short spectral fitting  
 176 window from 289 nm to 296 nm which is not affected by bright tropospheric clouds.

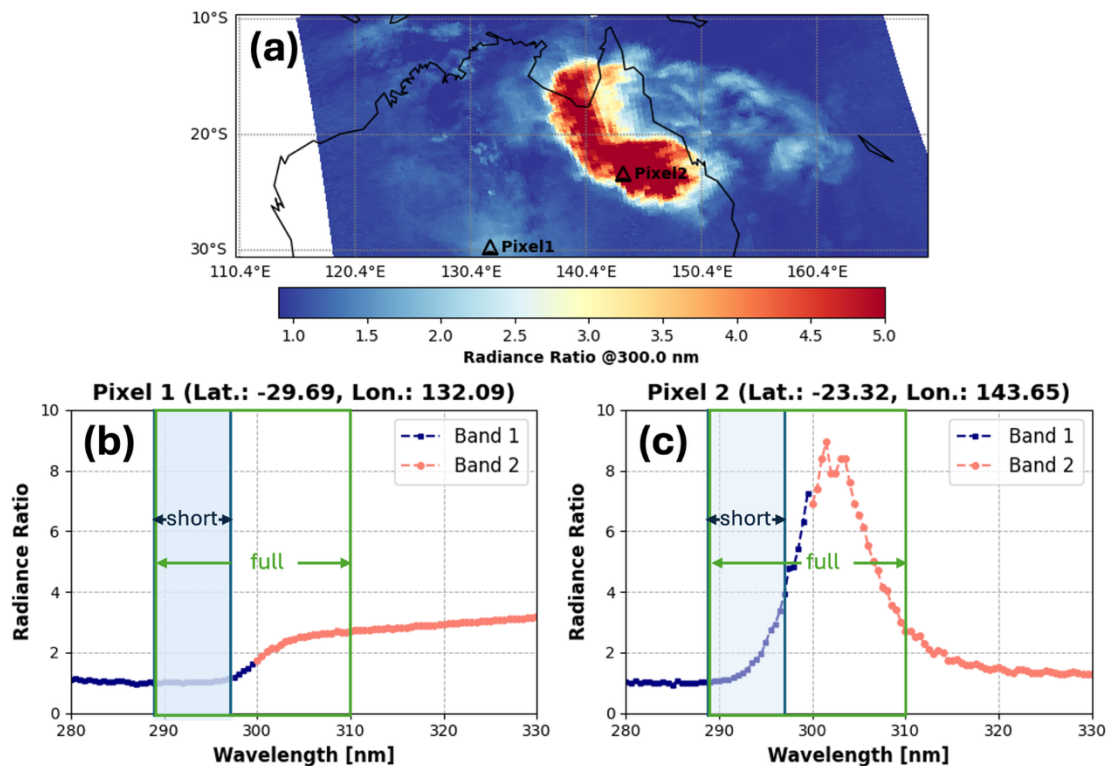


**Figure 3:** (a) Map of normalized TROPOMI radiance at 300 nm on January 17, 2022. Normalized TROPOMI radiance spectra for (b) a background (Hunga aerosol-free) Pixel 1 and (c) a Pixel 2 in the Hunga aerosol plume. The spectral radiance ratio plots indicate the coverage of TROPOMI UV bands 1 and 2 (with an overlap around 300 nm), as well as the ‘short’ and ‘full’ wavelength windows used for aerosol retrievals. Pixel 2 shows the typical enhancement of the radiance-ratio signal in the presence of stratospheric aerosols, whereas Pixel 1 shows the effect of tropospheric clouds, but only at longer wavelengths (>297 nm). Note that tropospheric clouds do not appear at short wavelengths (< 296 nm) (Pixel 1; lower left). We note that the separation between bands 1 and 2 occurs around ~300 nm, but it also depends on the across-track location.

177

178 For the 2-parameter (AOD and aerosol peak height,  $Z_p$ ) aerosol retrievals in Section 4, we restrict the spectral fitting window  
 179 from 289 nm to 296 nm (hereafter, denoted as the ‘short’ window) to reduce interference from bright tropospheric clouds.  
 180 Figure 3 shows radiance ratios (using TROPOMI orbit 22085 as background) over a large part of Australia, with six- to ten-  
 181 fold enhancements of the radiance-ratio signal in the presence of stratospheric aerosol. Background pixel ratios show signals  
 182 from tropospheric clouds, but ratios in the short wavelength window are free of such signals (Fig. 3; this is also seen in Fig.  
 183 2d, where cloud signals at wavelength 297.9 nm are apparent in the Australian Bight near the south-central coast).

184

185 Figure 4 presents spectral radiance ratio measurements at four selected wavelengths. At wavelengths shorter than 288 nm there  
 186 is no Hunga aerosol signature because of strong absorption by ozone above the Hunga plume altitude. The major plume  
 187 signature over Northeast Australia becomes much clearer for the longer wavelengths, 296 to 298 nm, but even at 292 nm (top  
 188 right) there is evidence of a forward plume streamer at high altitude over northwest Australia. Also of interest are the

189 tropospheric cloud echoes near the south-central Australian coast, evident at the two longer wavelengths (lower plots), but not  
190 present at shorter wavelengths. This indication has allowed us to set a cloud screening threshold at 296 nm. In Supplement S1,  
191 we present an animated video of the full spectral scan of TROPOMI band 1 and band 2 combined radiance ratios from 280 to  
192 330 nm in steps of 0.5 nm (<https://doi.org/10.5446/70186>).

193

194 We contour the Hunga stratospheric aerosol plume using a Cloud Screening Index (CSI), which is defined as a radiance ratio  
195 at 296 nm (see Appendix C for the CSI determination). Hereafter, we only consider TROPOMI pixels with  $CSI > 1.1$  for  
196 Hunga aerosol retrievals.

197 Note that we have also considered 3-parameter retrievals, with the third state vector element being the total column of  $SO_2$   
198 emitted simultaneously in the Hunga eruption; for this retrieval, we use the larger spectral fitting window (289–310 nm),  
199 denoted as the ‘full’ window in Figure 3. This retrieval takes advantage of strong  $SO_2$  absorption features present in TROPOMI  
200 Band 2 radiances (306–310 nm) but it does require the application of a cloud-correction step. This retrieval is currently under  
201 investigation.

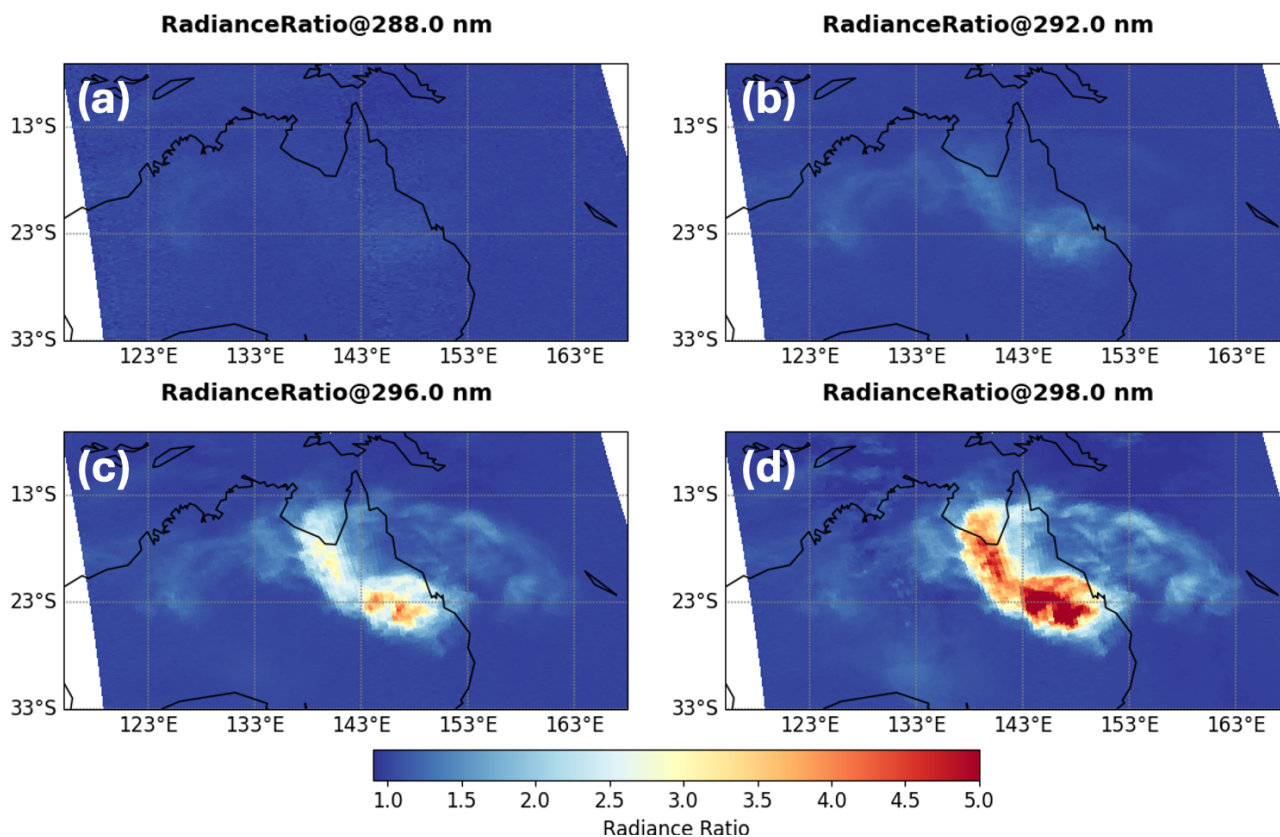


Figure 4: Radiance ratios (orbits 22086/22085 and 22087/22085) at (a) 288 nm, (b) 292 nm, (c) 296 nm, and (d) 298 nm. See the full spectral movie in Video Supplement S1 (<https://doi.org/10.5446/70186>).

## 203 2.2 Ozone Anomalies

204 As noted in the Introduction, we are motivated here to discuss the disruption in the BUV stratospheric ozone record due to the  
205 Hunga aerosols. Anomalies in a number of total ozone column (TOC) products were observed in the presence of the Hunga  
206 eruption plume; notably, enhanced BUV scattering signals due to high-altitude aerosol from the Hunga plume were mistakenly  
207 interpreted as TOC depletion in BUV ozone retrievals from all instruments (OMI, OMPS, GOME-2, as well as TROPOMI).  
208 Mid-stratospheric aerosols are not represented in the forward models used for the operational TOC retrievals, resulting in  
209 artificial TOC depletion during episodes of elevated volcanic aerosol loading. In this regard, it was necessary to re-analyze  
210 raw BUV spectra to flag pixels affected by the Hunga aerosols. Indeed, the presence of such ‘bad-quality’ ozone data will  
211 contaminate assimilation products that rely on BUV TOC data. For instance, artificially low BUV TOC data affected by Hunga  
212 plume resulted in anomalous assimilation outcomes in released M2-SCREAM reanalysis data (MERRA-2 Stratospheric  
213 Composition Reanalysis of Aura Microwave Limb Sounder (MLS) produced by NASA's Global Modelling and Assimilation  
214 Office using a stratospheric chemistry model and MERRA-2 meteorology (Gelaro et al., 2017; Wargan et al., 2023), as shown  
215 in Fig. 5a.

216

217 In contrast, ozone profile measurements from Microwave Limb Sounder (MLS) on board NASA Earth Observing System -  
218 chemistry (EOS Aura) satellite were not affected by the Hunga sub-micron aerosols with effective radii  $r_{eff} \sim 0.2-0.4 \mu m$   
219 (Boichu et al., 2023; Duchamp et al., 2023). Although stratospheric ozone profiles are strongly constrained by MLS,  
220 anomalously low OMI total ozone affects the ozone profile to some degree in the assimilated system, because data assimilation  
221 distributes the analysis increments in vertical levels according to a prescribed amount of background uncertainty. Also in this  
222 regard, there is some evidence (Evan et al. 2023; Zhu et al., 2023) of an actual physical ozone depletion inside the plume  
223 within days after the eruption.

224

225 For BUV aerosol plume retrievals, it is clear from the above discussion that we cannot use aerosol-contaminated BUV ozone  
226 data. Instead, for the air density, temperature, and ozone profiles, we have used specially-processed M2-SCREAM reanalysis  
227 data. This special processing involves the removal of erroneous OMI-retrieved total ozone columns in the Hunga plume from  
228 this reanalysis (both OMI and MLS are on the Aura platform) for the 10 day period of 15–25 January 2022. Figure 5b illustrates  
229 the total ozone map obtained from this special reprocessing and compares it to the original assimilated product. Assimilated  
230 ozone columns show a marked low anomaly over Northeast Australia when the assimilation system includes erroneous OMI  
231 TOC data (Fig. 5a). Filtering out the anomalous OMI TOC and performing the necessary reanalysis gives rise to a much  
232 smoother total ozone map (Fig. 5b). Assimilated ozone profiles have also shown low anomalies in the stratosphere when  
233 erroneous OMI TOC values were included (Fig. 5c). Regarding M2-SCREAM temperature profiles, early-January  
234 temperatures may be less reliable due to sparsely assimilated H<sub>2</sub>O and partial GPS radio-occultation contamination under

235 conditions of extreme moisture (Randel et al., 2023). To assess the reliability of these temperatures, we validated the M2-  
 236 SCREAM temperature profiles using radiosonde data from stations in Australia and New Caledonia (University of Wyoming  
 237 archive; <https://weather.uwyo.edu/upperair/sounding.shtml>). We selected eight cases in which the relative humidity exceeded  
 238 10% at least once above 15 km, including the January 17 2022 00 UTC sounding. The M2-SCREAM temperatures agreed  
 239 with the radiosonde measurements within  $\sim 4$  K over 15–30 km range, supporting that the re-analyzed M2-SCREAM  
 240 temperature profiles are sufficiently reliable for interpreting the early Hunga plume conditions.  
 241

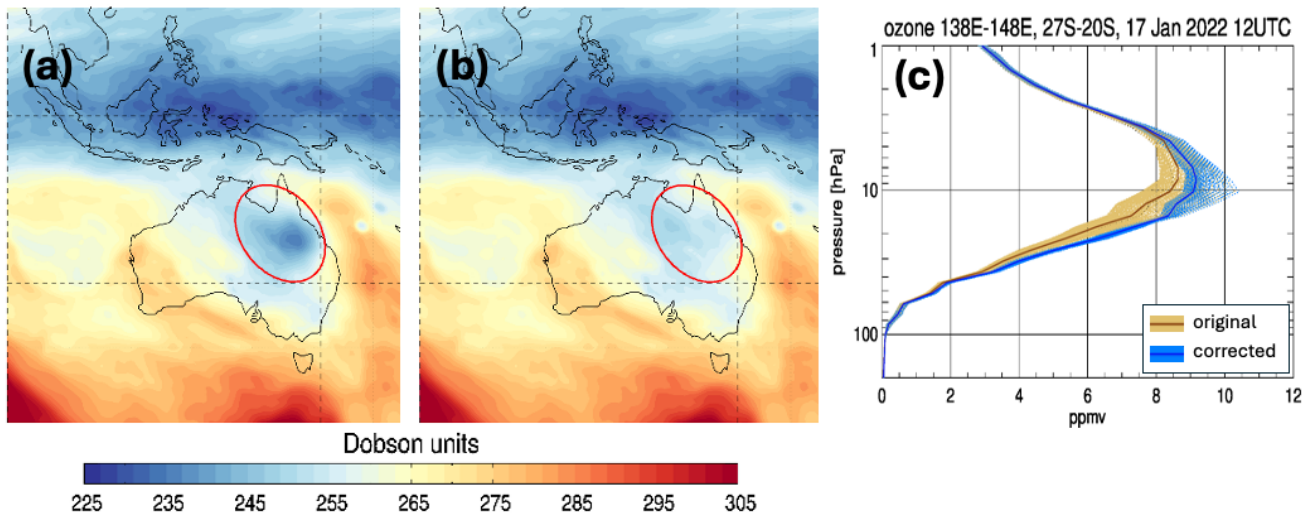


**Figure 5: Spatial distribution of TOC in M2-SCREAM reanalysis data on January 17, 2022 at 6 UTC. (a) Assimilation using anomalous OMI V3 TOC retrievals. (b) Assimilation after filtering out the anomalous OMI TOC re-processed M2-SCREAM. (c) Ozone profiles from the original M2-SCREAM reanalysis data (orange), and from the assimilation that omitted anomalous OMI TOC (blue) on January 17, 2022 at 12 UTC.**

### 242 3. The Hunga Nadir-BUV Aerosol Retrieval Algorithm

243 In Section 3.1 we introduce measurement and state vectors, focusing on the use of ratioed BUV radiances from adjacent orbits;  
 244 this section deals with parameterization of the Hunga plume in terms of a pseudo-Gaussian profile shape. We summarize the  
 245 deployment of the VLIDORT Radiative Transfer (RT) model in the forward model component in Section 3.2, with special  
 246 emphasis on the linearized optical property set-ups required by VLIDORT to generate analytically-derived Jacobians with  
 247 respect to AOD and peak height. The least-squares inversion model is outlined in Section 3.3, and in Section 3.4, we discuss  
 248 the preparation of aerosol optical properties, parameterization of the  $\text{SO}_2$  vertical profile, and the use of input ozone profiles  
 249 from the modified MERRA-2 reanalysis. Section 3.5 is concerned with algorithm validation using synthetic data.

#### 250 3.1 Retrieval Algorithm: State and Measurement Vectors

251 Measurement vectors for the retrieval are ratios of two TROPOMI Earthshine spectra (Eq. 3.1):

252

253

254

255

256

257

258

259

260

261

262

263

264

265

266

267

268

269

270

271

272

273

274

275

276

277

278

279

280

$$M_{meas}(\lambda) = \frac{R_{meas}^{(Volc)}(\lambda)}{R_{meas}^{(Bkgd)}(\lambda)}. \quad (3.1)$$

Here, the quantity  $R_{meas}^{(Volc)}(\lambda)$  is a TROPOMI spectrum with a clearly-pronounced volcanic aerosol signal (e.g., from orbit 22086), and  $R_{meas}^{(Bkgd)}(\lambda)$  is a similar spectrum from an adjacent background aerosol-free TROPOMI orbit (orbit 22085). As noted in Section 2.2, the key assumption is that the re-processed M2-SCREAM stratospheric ozone and temperature profiles are accurately characterized regardless of the presence of Hunga aerosols. We also examined the potential impact of possible air-density variations that may not be fully captured by the M2-SCREAM reanalysis during the early days after the eruption. Such differences could influence Rayleigh scattering (Bodhaine et al., 1999) and the scaling of ozone absorption (Guo and Lu, 2006), since both depend on air density. Geolocations for each spectrum in the orbit pair are very similar, and we assume the same wavelength grid for both orbits.

The dimension of the measurement vector is variable – this depends on the choice of spectral fitting window and the application of spectral smoothing (if any). For the short window (289–296 nm), there are typically 107 spectral points without smoothing.

For errors on the measurements, we take radiance noise levels from the TROPOMI Level 1b product, assuming individual measurement errors to be uncorrelated. The uncertainty in the radiance ratio is then calculated using error propagation, combining the relative uncertainties of each scene in quadrature and scaling the result by the radiance ratio.

The number of retrieved quantities determines the dimension of the state vector. The Hunga aerosol loading profile  $\{E(z)\}$  as a function of altitude  $z$  is taken to have a ‘pseudo-Gaussian’ shape (this analytic parameterization is sometimes called a Generalized Distribution Function), characterized by three parameters  $\{A_0, z_p, h_w\}$ . Here,  $A_0$  is the Hunga stratospheric AOD at a fixed reference wavelength  $\lambda_{ref}$  (taken to be 312 nm),  $z_p$  is the plume peak height in [km], and  $h_w$  is the half-width-half-maximum of the plume profile (also in [km]). For our 2-parameter retrieval, the state vector is  $x = \{A_0, z_p\}$ , with  $h_w$  treated as a known model parameter (see Section 3.4 for more on this quantity). Appendix A contains a description of this pseudo-Gaussian parameterization, including explicit analytic expressions for  $E(z; A_0, z_p, h_w)$  in terms of the three parameters of interest, and a determination of analytic derivatives  $\left\{\frac{\partial E(z)}{\partial A_0}, \frac{\partial E(z)}{\partial z_p}\right\}$  necessary for deriving Jacobian output from the forward model component of the retrieval algorithm.

281 **3.2 Forward Model Radiative Transfer (RT) and Analytic Jacobians**

282 Next, we consider the forward-model RT simulation of the ratioed BUUV spectra. The retrieval algorithm requires forward-  
 283 model Jacobians with respect to state vector elements; here, the 2-parameter vector  $x = \{A_0, z_p\}$ . In general, the forward model  
 284 will generate simulations  $M_{sim}(\lambda)$  to match the quantities in Eq. (3.1). This requires two RT simulations:  $R_{sim}^{(Bkgd)}(\lambda)$  is the  
 285 RT calculation for a background atmospheric scenario with no aerosol, and  $R_{sim}^{(Volc)}(\lambda)$  is RT simulation with similar  
 286 background, but including the aerosol plume. In addition to  $M_{sim}(\lambda)$ , the forward model must also generate Jacobians with  
 287 respect to the aerosol parameters:

288

$$289 \quad K(\lambda) \equiv \left[ \frac{\partial M_{sim}(\lambda)}{\partial A_0}, \frac{\partial M_{sim}(\lambda)}{\partial z_p} \right] = \frac{1}{R_{sim}^{(Bkgd)}(\lambda)} \cdot \left[ \frac{\partial R_{sim}^{(Volc)}(\lambda)}{\partial A_0}, \frac{\partial R_{sim}^{(Volc)}(\lambda)}{\partial z_p} \right]. \quad (3.2)$$

290

291 We use the VLIDORT discrete-ordinate RT model for simulating polarized light fields (Spurr, 2006; Spurr and Christi, 2019)  
 292 for the two forward-model calculations required for these measurements of ratioed backscatter.  $R_{sim}^{(Bkgd)}(\lambda)$  is a simulation for  
 293 a Rayleigh scattering atmosphere with O<sub>3</sub> absorption, and no aerosols or SO<sub>2</sub>; the O<sub>3</sub> profile is from assimilation constrained  
 294 by MLS and corrected OMI measurements, as described in Section 2.2. The major advantage with VLIDORT is its  
 295 simultaneous ability to generate not only the radiance fields, but also any set of analytically-derived Jacobians (weighting  
 296 functions) with respect to atmospheric or surface parameters.

297

298 Aerosol optical properties are required for the  $R_{sim}^{(Volc)}(\lambda)$  simulation based on a pseudo-Gaussian aerosol plume loading; for  
 299 this, we use a linearized Mie scattering model (Spurr et al., 2012) to develop these properties from assumed knowledge of  
 300 Hunga aerosol microphysical quantities (refractive index, particle size distribution parameters). Details of the aerosol optical  
 301 property Mie derivations are found below in Section 3.4, along with a discussion of other atmospheric constituent profiles (in  
 302 particular, O<sub>3</sub> and SO<sub>2</sub>). VLIDORT requires total optical properties and their corresponding linearization to compute the  
 303 Jacobians (see Appendix B for details).

304 **3.3 Inverse model**

305 The retrieval inverse model is an iterative damped non-linear least-squares minimization using a modified version of the  
 306 Levenberg-Marquardt (L-M) algorithm (LMA) (Marquardt, 1963) with variable step-size (see e.g., Chong and Zak, 2001). If  
 307  $x_m$  is the state vector at iteration  $m$ , then the estimate for the state vector at the next iteration is given by:

308

$$309 \quad x_{m+1} = x_m + \alpha_m (K^T S_\epsilon^{-1} K + \mu_m I)^{-1} K^T S_\epsilon^{-1} (y_{meas} - F(x_m)) \quad (3.3)$$

310

311 Here,  $K$  is the Jacobian matrix which has row vector  $K(\lambda_i)$  for wavelength  $\lambda_i$  in the fitting window as seen in Eq. (3.2),  $y_{meas}$   
 312 is the measurement vector with entries  $M_{meas}(\lambda_i)$  (Eq. (3.1)),  $F(x_m)$  is the forward-model simulated measurement vector with  
 313 entries  $M_{sim}(\lambda_i)$  of the same form as that in Eq. (3.1),  $S_\epsilon$  is the measurement and forward-model error covariance matrix (here  
 314 considered diagonal), and  $I$  is the identity matrix. The “T” superscript denotes matrix transpose. This inversion scheme is a  
 315 form of the maximum-likelihood (ML) method (Rodgers, 2000).

316  
 317 The L-M damping parameter  $\mu_m$  is adjusted as needed at each iteration in order to ensure the approximation to the Hessian  
 318 matrix ( $K^T S_\epsilon^{-1} K + \mu_m I$ ) in Eq. (3.3) remains positive definite. This ensures that the shape of the cost-function approximation  
 319 we are seeking to minimize during that iteration is “bowl-shaped”, and that the negative of the gradient  $K^T S_\epsilon^{-1} (y_{meas} -$   
 320  $F(x_m))$  in Eq. (3.3) points in a direction to descend into the bowl.

321  
 322 The step-size  $\alpha_m$  is sometimes determined by a line search, in order to *guarantee* the cost function approximation is minimized  
 323 at each iterative step; however, this procedure would be too numerically expensive in our retrieval. Instead, in order to ensure  
 324 that  $A_0$  and  $z_p$  remain in physical parameter space at each iteration step, we simply halve the step size repeatedly until this  
 325 physicality condition is satisfied (starting at  $\alpha_m = 1$ ).

326  
 327 Convergence is reached when relative differences in state-vector elements between adjacent iterations are all below a threshold  
 328 criterion ( $10^{-2}$  in our case), and/or when the cost-function itself reaches a clear minimum in fitting space. Spectral points are  
 329  $\{\lambda_i\}$ ,  $i = 1, \dots, N_s$ , where the number of points  $N_s$  depends on the selection of TROPOMI measurements in UV band 1. With  
 330 two parameters ( $A_0$  and  $Z_p$ ), matrix  $K$  in Eq. (3.3) has dimension  $N_s \times 2$ .

331  
 332 In addition to the above, to obtain *better* estimates of uncertainties on the retrieved state vector elements  $A_0$  and  $z_p$ , a facility  
 333 was implemented to modify the original standard deviations from the measurement and forward-model error covariance matrix  
 334  $S_\epsilon$  used in retrieval (which is often based initially on measurement characteristics alone such as signal-to-noise ratio (SNR)).  
 335 This was done as follows. As part of each original retrieval, a chi-square diagnostic  $\chi^2 = [y_{meas} - F(x)]^T S_\epsilon^{-1} [y_{meas} - F(x)]$   
 336 is produced. If the value of chi-square for the retrieval is too large - indicating that the estimated mismatch in actual  
 337 measurements  $y_{meas}$  versus forward-model-simulated measurements  $F(x)$  is generally too large relative to that assumed using  
 338 the original standard deviations in  $S_\epsilon$  - then the *expected value* of chi-square for the retrieval (i.e., the number of measurements  
 339  $n$  used in the retrieval minus one), along with  $y_{meas}$ , the final values of  $F(x)$  from the original retrieval, and the original  
 340 standard deviations used in  $S_\epsilon$ , are used to compute an additional contribution to the estimated standard deviation of  
 341 measurement/forward model error for each measurement. These contributions help to account for the influence of unknown  
 342 sources of measurement and/or forward model error. These values are then added to the original measurement standard  
 343 deviations on the diagonal of  $S_\epsilon$  and the retrieval is then *re-run* using the more realistic combined standard deviations of

344 measurement and forward-model error. With this procedure, retrieved values of the state vector elements often do not change  
 345 significantly, but their estimated uncertainties are often more realistic (i.e., larger), along with improved chi-square diagnostics.  
 346

### 347 3.4 Aerosol optical properties, trace gas profiles and parameterizations, forward-model setups

#### 348 Background profiles

349 As noted in Section 2.2, we use specially-processed ozone and temperature assimilated vertical profiles (reprocessed M2-  
 350 SCREAM) – this data set contains pressure, temperature and ozone volume mixing ratios specified for a 72-layer vertical grid  
 351 at 1–2 km vertical resolution in the stratosphere. This 72-layer grid forms the basis for the atmospheric stratification. We have  
 352 imposed a finer vertical resolution for the Hunga aerosol plume (typically 0.25 km is sufficient), in order to properly  
 353 characterize the pseudo-Gaussian plume shape. Baseline retrievals are done assuming the aerosol peak height  $Z_p$  to be between  
 354 24 and 34 km, in general above the ozone density peak at ~25 km. We performed a sensitivity study allowing the minimum  
 355 value of  $Z_p$  to be 20 km; we found that this had a negligible impact on the total aerosol mass retrieval. Figure 6 illustrates the  
 356 assumed aerosol and ozone profile distributions, along with CALIOP overpasses from January 17, 2022. In particular, the  
 357 CALIOP daytime overpass at 5:29 UTC shows a narrow plume at 30 km (Fig. 6c, see also the CALIOP nighttime overpass at  
 358 ~16:20 UTC (Fig. 6d) and ~17:59 UTC (Fig. 6e)); based on this, we estimate a plume half-width of ~0.4 km, and this value  
 359 was assumed throughout the retrievals discussed in the paper. The CALIOP data were used to validate our retrievals (see  
 360 Section 4.4).

361

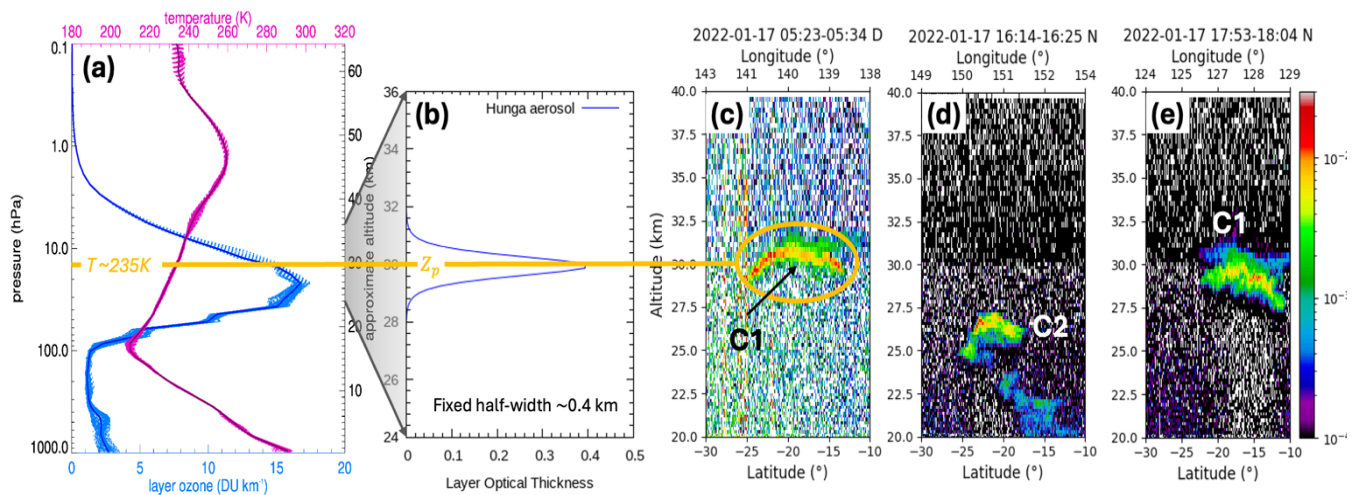


**Figure 6: (a) Ozone and temperature profiles from the reprocessed M2-SCREAM reanalysis data on January 17, 2022, at 12 UTC. (b) Example of a modelled aerosol profile assuming a Gaussian-like shape with fixed half-width ~0.41 km (see Appendix A). (c) Total attenuated backscatter at 532 nm measured by CALIOP during daytime (~5:29 UTC) on January 17, 2022. Same as Fig. 6c but for nighttime measurements at (d) ~16:20 UTC and (e) ~17:59 UTC.**

362 Optical Properties

363 The Mie code is an integral part of the forward model; we use the code to generate aerosol optical properties in the UV range,  
364 based on microphysical inputs typical for stratospheric sulfuric acid solution spherical droplets (Palmer and Williams, 1975;  
365 Beyer et al., 1996). These inputs include laboratory measurements of complex index of refraction at a reference wavelength  
366 of 312 nm, for a binary sulfuric acid H<sub>2</sub>SO<sub>4</sub>/H<sub>2</sub>O solution. We have chosen two values for the real part of the refractive index  
367 ( $n_r=1.39$  and  $n_r=1.47$ ), which represent the lower and upper limits of the laboratory measurements (Beyer et al., 1996) which  
368 correspond to low ( $w = 0.291$ ) and high ( $w = 0.765$ ) acid mass fractions of the binary water-sulfuric acid solutions (Myhre  
369 et al., 1998). This wide range for the real part of the refractive index reflects the plume composition simulated by NASA  
370 Goddard Earth Observing System (GEOS) Earth system model (see Appendix F), i.e., H<sub>2</sub>SO<sub>4</sub> wt% spanning roughly 40–70%  
371 (core values ~40%) and thus reasonably bracketing the ~30–80% range. We assumed  $n_r$  values to be spectrally unvarying. The  
372 imaginary part of the refractive index can be neglected in the UV, visible and near infrared wavelengths (Beyer et al., 1996);  
373 this was set to a value of  $10^{-4}$  throughout.

374

375 Besides complex refractive index values  $\{n_r, n_i\} = \{1.39, 10^{-4}\}$  and  $\{1.47, 10^{-4}\}$ , two parameters — the fine mode radius  
376 ( $R_g \sim 0.14 \mu\text{m}$ ) and the standard deviation ( $S_g = 1.545$ ) of the particle number size distribution — were chosen to characterize  
377 the unimodal lognormal particle number size distribution of the Hunga aerosol; these parameters were taken from the Lucinda  
378 AERONET level 1.5 (Holben et al., 1998) sun-sky radiance inversions (Dubovik and King 2000) during Hunga cloud overpass  
379 (Boichu et al., 2023). An initial call to the Mie program is required to generate the extinction coefficient  $Q_{ext}(\lambda_0)$  at reference  
380 wavelength  $\lambda_0 = 312$  nm, and this is followed by more calls to the Mie code at every spectrum wavelength to generate the full  
381 set of aerosol optical properties (spectral extinction, single scattering albedo, elements of the scattering matrix) required as  
382 input to the VLIDORT optical setup. The deployment of these Mie properties in the VLIDORT setup is discussed in Appendix  
383 B.

384

385 Ozone cross-sections are taken from laboratory measurements (Brion et al., 1993). The original high-spectral resolution data  
386 are pre-convolved with pixel-specific spectral response functions and then spline-interpolated to TROPOMI wavelengths. SO<sub>2</sub>  
387 cross-sections are taken from Bogumil et al. (2003) and are also pre-convolved and interpolated. Both cross-section data sets  
388 have quadratic-parameterized temperature dependencies based on re-processed M2-SCREAM assimilated temperature profiles  
389 (Fig. 6a). Rayleigh scattering cross-sections and depolarization ratios are taken from a standard source (Bodhaine et al., 1999).

390

391 Radiative Transfer Aspects

392 In the UV spectral region below 300 nm, single scattering (SS) dominates the RT for an aerosol-free stratosphere, with light  
393 penetration depths related to the wavelength-dependent ozone absorption peaks. With high-altitude Hunga aerosols present,  
394 multiple scattering (MS) becomes more important, and it is necessary to run VLIDORT in full scattering mode (SS + MS).  
395 The number of discrete ordinates is set at 8 in the polar angle half space; we have found that this is sufficient for treating the

396 Hunga aerosol scattering accurately, provided the delta-M scaling approximation is in force. VLIDORT is run in linear  
397 polarization mode (Stokes-vector components  $I, Q, U$ ); circular polarization is neglected.

### 398 **3.5 Validation with synthetic data**

399 We calculated Hunga BUV synthetic radiances using the NASA OMI spectral simulator software, based on geophysical  
400 conditions for January 17, 2022. Simulations were performed with and without aerosols to develop synthetic radiance ratios,  
401 which were then used as input to the Hunga inversion tool, the purpose being to evaluate the impact of changing the ozone  
402 profile and the Hunga aerosol layer height and AOD. These tests helped to develop confidence in the forward and inverse  
403 models used in the real Hunga retrievals.

404  
405 In addition, a number of tests were carried out to obtain a sense of the retrieval's sensitivity to (1) the half width at half  
406 maximum (HWHM) of the ascribed aerosol plume profile, (2) profiles of atmospheric density and ozone, (3) parameters  
407 governing the aerosol particle size distribution [e.g. mode fraction (assuming a bimodal particle size distribution), mode radius,  
408 refractive index (real & imaginary parts)], (4) the spectral window chosen for retrieval, and (5) the influence of the initial state  
409 vector guess on retrieval convergence. These tests were used as a guide to aspects of the retrieval which demanded further  
410 attention during the process of refining the retrieval algorithm.

411  
412 To further verify the fidelity of the retrieval algorithm itself, we performed a set of closed-loop validation tests using synthetic  
413 radiance spectra generated by the forward model. Each test used a pre-defined state vector  $X_{true} = \{AOD, Z_p\}$  to represent  
414 typical post-eruption conditions. Two cases were examined: (1) a retrieval based on noise-free synthetic spectra to ensure that  
415 the algorithm could reproduce the known state ( $X_{ret} \approx X_{true}$ ), and (2) a retrieval using spectra with added random noise levels  
416 representative of TROPOMI UV band 1 measurements to assess retrieval robustness under realistic conditions. In both cases,  
417 the retrieved parameters converged closely to the true inputs, demonstrating that the Hunga retrieval framework is stable and  
418 internally consistent. The noise-added tests also showed slightly larger retrieval uncertainties, as expected, but without  
419 systematic bias in AOD or  $Z_p$ . Overall, the results increased confidence in the forward and inverse model configurations used  
420 in the actual Hunga plume retrievals.

### 421 **4. Hunga Aerosol Retrieval Results**

422 To facilitate Hunga stratospheric aerosol column mass estimation, we have selected TROPOMI measurements from 17 January  
423 2022, taken at ~1:30 pm local time (03:30 UTC), because by that time (~47 hours after the eruption) the SO<sub>2</sub>/sulfate aerosol  
424 clouds have completely separated from the ash and ice clouds (see Fig. 1c from Sellitto et al., 2022), but the volcanic clouds  
425 were still above the ozone density peak at ~25 km. The absence of UV-absorbing ash is confirmed by low values of the

426 TROPOMI-derived UV absorbing aerosol index. As noted in section 2.1, Hunga plume pixels have been discriminated using  
427 a cloud screening index (CSI) value greater than  $> 1.1$ , where CSI is the BUV radiance ratio with the background orbit (22085)  
428 at 296 nm (see Appendix C).

#### 429 **4.1 Aerosol Peak Height Retrievals**

430 Hunga aerosol peak heights  $Z_p$  were retrieved using both lower ( $n_r = 1.39$ ) and upper ( $n_r = 1.47$ ) bounds of the real part of the  
431 refractive index; these values provide an uncertainty range for Hunga  $Z_p$  retrievals. Figure 7a shows  $Z_p$  retrieved using the  
432 upper-bound index ( $n_r = 1.47$ ). The highest values of  $Z_p > 30$  km were retrieved in the western part of the plume from orbit  
433 22087. The lower  $Z_p$  values ( $\sim 25$  km) were retrieved in the eastern part from orbit 22086. This west–east contrast is consistent  
434 with previous studies distinguishing the western aerosol- and water-rich cloud (C1) and the eastern  $\text{SO}_2$ -rich cloud (C2) (Carn  
435 et al., 2022; Legras et al., 2022). The C1 cloud likely experienced faster  $\text{SO}_2$ -to-sulfate conversion and stronger water-driven  
436 radiative cooling, which contributed to its more rapid descent compared to that for C2, as noted in previous analyses (Legras  
437 et al., 2022; Sellitto et al., 2022). This difference is largely explained by the strong stratospheric easterly wind gradient in the  
438 20–40 km altitude range. This interpretation is supported by the trajectory analysis presented in Appendix D, which uses  
439 assimilated wind data from the MERRA-2 reanalysis. The higher the altitude, the stronger the easterly winds, so those parts of  
440 the C1 cloud at  $Z_p \sim 30 \pm 1$  km were advected westward more quickly than the lower parts (Sadeghi et al., 2025). By contrast,  
441 the C2 cloud, centered near  $Z_p \sim 25 \pm 1$  km in the eastern sector, showed slower westward advection consistent with a weaker  
442 easterly wind field at these lower stratospheric levels.

443  
444 We compared the TROPOMI aerosol peak heights  $Z_p$  retrieved from orbit 22086 at  $\sim 3:30$  UTC and orbit 22087 at  $\sim 5$  UTC  
445 with the CALIOP daytime overpass at 5:27–5:29 UTC (Fig. 7b) and later nighttime overpass at  $\sim 16:16$  UTC (Fig. 7c).  
446 Examining the daytime CALIOP data, we see that the average height of the C1 cloud is close to 30 km. The  $Z_p$  heights retrieved  
447 from TROPOMI orbit 22087,  $\sim 30$  minutes prior to the CALIOP observations, match within  $\sim 1$  kilometer. A second validation  
448 was obtained with the CALIOP nighttime overpass at 16:16 UTC (solid magenta line), where matchup between CALIOP and  
449 TROPOMI pixels within the C2 part of the Hunga plume (shown with the dashed magenta line) can be achieved with 13-hour  
450 back trajectories (Appendix D).

451  
452 TROPOMI  $Z_p \sim 30$  km over the northeast part of Australia also agrees with the geometric top height retrievals from the Multi-  
453 angle Imaging Spectro-Radiometer (MISR) aboard NASA's Terra satellite. On January 17, 2022, MISR observed the Hunga  
454 aerosol plume off the northeast coast of Australia at  $\sim 00:25$  UTC, with retrieved values of 27–30+ km ASL (30 km is the  
455 maximum allowed retrieval height in the MINX (MISR Interactive EXplorer) stereo-height retrieval (Kahn et al., 2024).

456

457 Figure 7d shows the absolute difference in  $Z_p$  retrieved using the lower-bound refractive index ( $n_r=1.39$ ) relative to  $n_r=1.47$   
 458 scenario. The average difference is  $0.03 \pm 0.8$  km, indicating generally low sensitivity to the refractive index assumptions.  
 459 Notably, in the central dense part of the plume, most areas fall within a  $\pm 1$  km difference range (shaded in gray). However,  
 460 larger localized differences of up to  $\pm 2$  km were observed in the eastern part of the plume above the Coral Sea. These  
 461 discrepancies may be due to the low altitude of the Eastern part of the plume, close to the assumed plume boundary (24 km).  
 462  $Z_p$  differences up to  $\sim 4$  km were found in areas with thin aerosol layers, likely due to reduced sensitivity in such cases. Overall,  
 463 differences in  $Z_p$  values retrieved using extreme refractive index assumptions fall within the expected range.

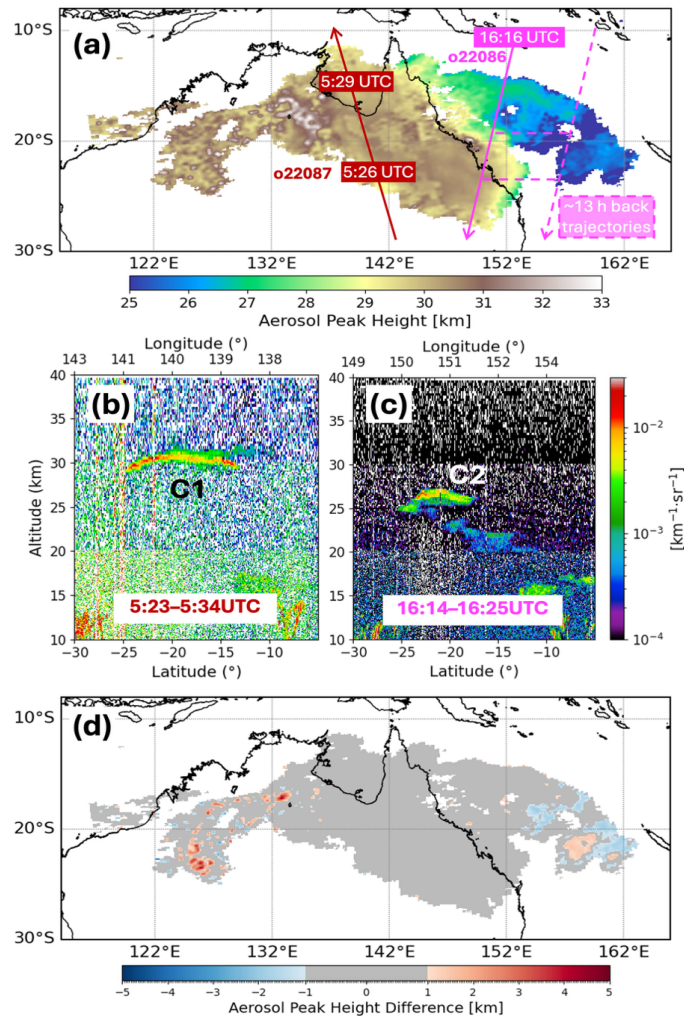


**Figure 7:** (a) Retrieved aerosol plume peak height  $Z_p$  [km] assuming upper limit refractive index  $n_r = 1.47$ , from TROPOMI orbits 22086 ( $\sim 3:20$  UTC) and 22087 ( $\sim 5$  UTC) on January 17, 2022. The dashed magenta line shows a back-trajectory matchup between nighttime CALIOP measurements and daytime TROPOMI Hunga aerosol retrievals. (b) The CALIOP attenuated backscatter during daytime ( $\sim 5:23\text{--}5:34$  UTC) with the ground track shown in panel (a) with the solid red line. (c) Same as (b) but for a nighttime track ( $\sim 16:14\text{--}16:25$  UTC), which is shown with the solid magenta line in panel (a). (d) Absolute difference in retrieved  $Z_p$  assuming low ( $n_r=1.39$ ) and high ( $n_r=1.47$ ) refractive index scenarios.

464 **4.2 Aerosol Optical Depth Retrievals**

465 To assess the sensitivity of the AOD retrieval to the assumed real part of the aerosol refractive index, we performed retrievals  
 466 using low and high values of  $n_r$  (1.39 and 1.47), which span the plausible range for sulfuric acid aerosols. Figure 8 shows  
 467 TROPOMI-retrieved AOD at reference wavelength 312 nm for the upper limit of the refractive index ( $n_r = 1.47$ ) and the  
 468 percentage difference in results between the two  $n_r$  scenarios. The highest AOD values (up to  $\sim 5.0$ ) were retrieved over the  
 469 Coral Sea (C2 cloud), where the densest portion of the volcanic plume was concentrated at lower plume altitudes around 25  
 470 km (see Fig. 8a). As the plume was transported westward across northern Australia, a secondary maximum in aerosol density  
 471 was located over Western Queensland (C1 cloud), with AOD values as high as 3. Further westward, AOD values gradually  
 472 decreased over Northeast Australia coinciding with a higher  $Z_p$  values ( $> 30$  km).

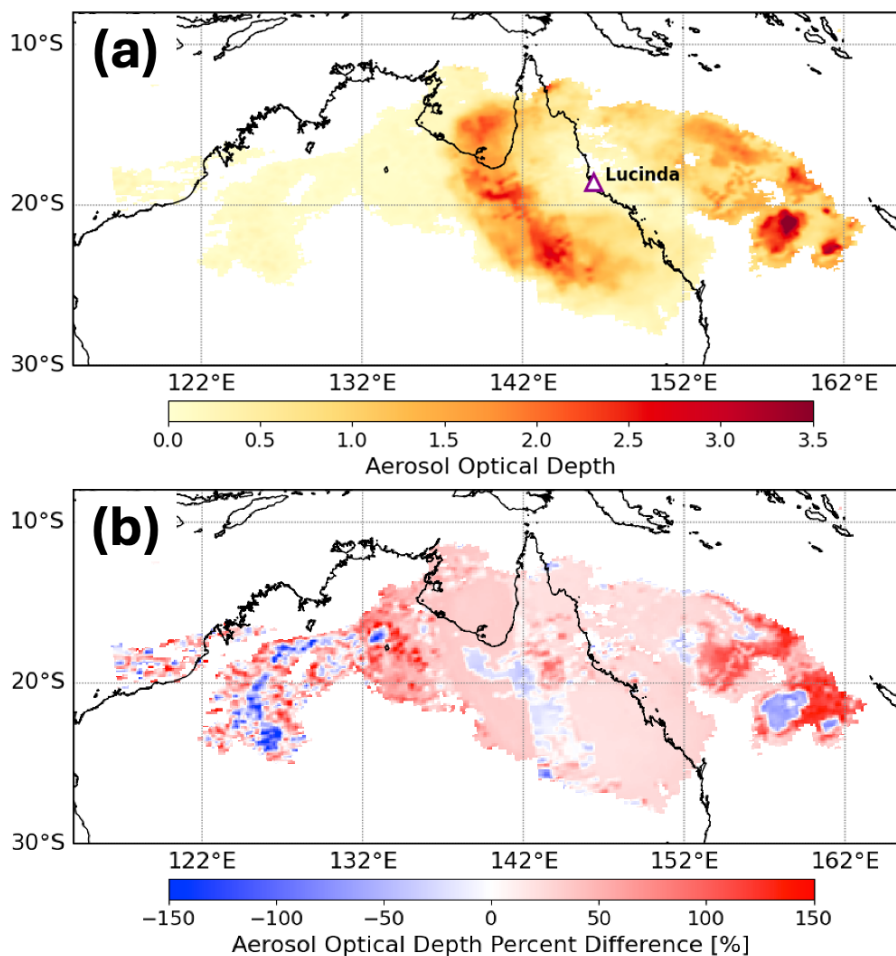


Figure 8: (a) Retrieved TROPOMI Aerosol Optical Depth assuming  $n_r = 1.47$  at 312 nm for orbits 22086 and 22087. The location of the Lucinda AERONET site is marked with a triangle. (b) Percentage difference in AOD values between two refractive index scenarios ( $n_r = 1.39$ ,  $n_r = 1.47$ ) calculated relative to the  $n_r = 1.47$  case.

473

474 The comparison (Fig. 8b) shows that retrieved AODs for low aqueous sulfuric acid solution concentration ( $n_r = 1.39$ ) are  
475 generally higher than those AODs for high solution concentration ( $n_r = 1.47$ ), with a mean percent difference of  $\sim 30\%$ ; this  
476 provides an estimate of the AOD systematic retrieval error associated with uncertainties in the refractive index assumptions.  
477 The largest differences were found in regions with optically thick plumes, particularly over the Coral Sea, where the aerosol  
478 peak height was close to the assumed low limit of  $Z_p \sim 24$  km — that is, close to the ozone density peak.

479  
480 To validate our TROPOMI AOD retrievals, we compared them with AERONET direct-sun AOD measurements (Holben et  
481 al., 1998) from the Lucinda coastal site (18.5198°S; 146.3861°E; elevation: 8.0 m) during the Hunga plume overpass from  
482  $\sim 21$  UTC on January 16 to  $\sim 03$  UTC on January 17 (Fig. 9). The Lucinda site is located  $\sim 6$  km offshore in the tropical coastal  
483 waters of the Great Barrier Reef, and background AOD at this site is typically very small. Based on AERONET values of  
484 aerosol microphysical parameters and assumed values of refractive index, we used the Mie code to convert our retrieved  
485 TROPOMI AOD at 312 nm to corresponding quantities at 412 nm; this is the shortest AOD wavelength for AERONET  
486 measurements at Lucinda (Fig. 9b). We also subtracted tropospheric AOD contributions of 0.1, as measured by AERONET  
487 on previous days to the Hunga plume overpass.

488  
489 Using the NASA Goddard trajectory model (see Appendix D), we calculated the backward movement of air parcels starting  
490 from TROPOMI AOD retrievals from orbit 22087 (overpass at 05:00 UTC) and from 22086 (overpass at 03:15 UTC). We  
491 averaged all TROPOMI AOD retrievals from those parcels that pass within 10 km of the Lucinda site and compared them with  
492 the AERONET AOD measurements averaged over a 15-minute interval (Fig. 9a). We see that average retrieved AOD values  
493 show good qualitative agreement with the AERONET AOD measurements. Quantitatively, the retrievals assuming  $n_r = 1.47$   
494 (black dotted curve) showed a median difference of 0.25 (mean: 0.3) relative to AERONET. For the  $n_r = 1.39$  (black solid  
495 curve) case, the median difference is similar 0.3 (mean: 0.3). Both TROPOMI and AERONET AODs reached a maximum  
496 (over 2) during the local-time morning hours (21:45–23:00 on Jan 16 UTC) and dropped to  $\sim 0.5$  after the main part of the  
497 Hunga aerosol cloud passed over the station.

498  
499 TROPOMI AOD retrievals also agree qualitatively with MISR-retrieved  $\text{AOD}_{558} \sim 0.7 \pm 0.2$  ( $1\sigma$ ) (Kahn et al., 2024),  
500 accounting for spectral differences in the aerosol extinction between short UV and mid-visible wavelengths (Fig. 9b). Recent  
501  $\text{AOD}_{532}$  retrievals from CALIOP nighttime Hunga overpasses estimate somewhat larger  $\text{AOD}_{532}$  values of  $\sim 1.24 \pm 0.13$  ( $1\sigma$ )  
502 for C1 and  $\sim 1.01 \pm 0.12$  ( $1\sigma$ ) for C2 on January 17 (Duchamp et al., 2025). These CALIOP-derived  $\text{AOD}_{532}$  values are also  
503 qualitatively consistent with TROPOMI AOD results, considering the spatial heterogeneity of the Hunga plume, the temporal  
504 differences between the satellite overpasses, and the spectral differences between the retrievals. A more comprehensive  
505 comparison with CALIOP will be conducted in a follow-up study.

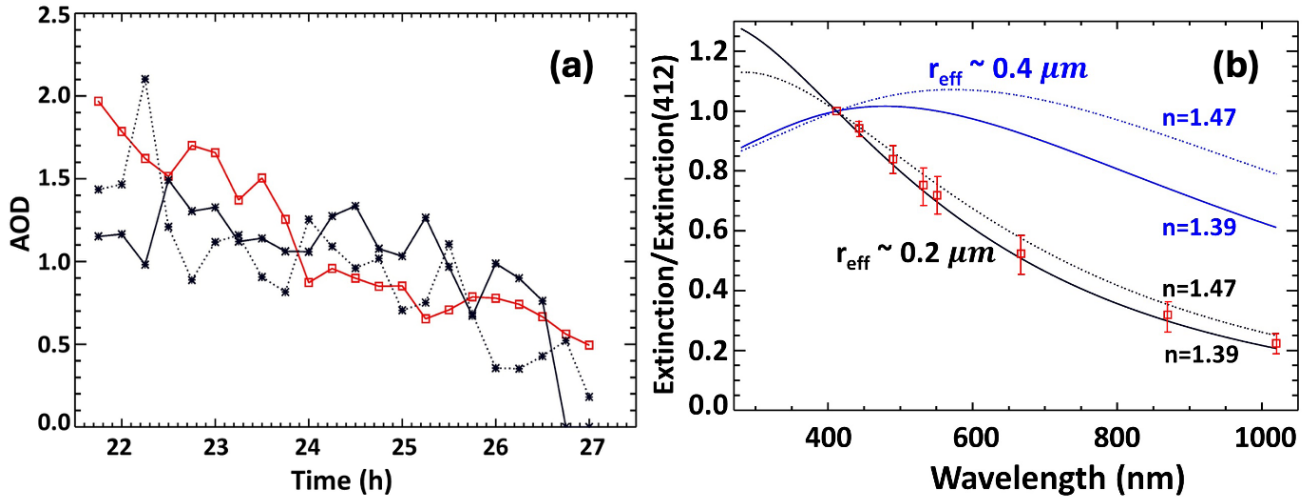
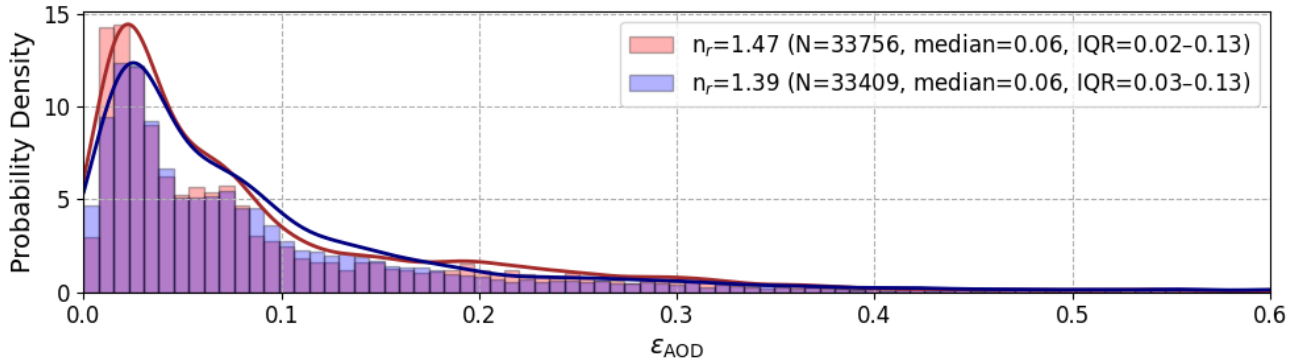


Figure 9: Panel (a) red line shows 15-minute averages of the AERONET AOD<sub>412</sub> measurements at 412nm at Lucinda site started at 21:45 UTC on 16 January 2022 (local morning time) and continued until ~ 03:00 UTC on January 17, 2022. The horizontal scale is given in hours elapsed from 00:00UTC on January 16. We subtracted a background tropospheric AOD of 0.1 measured on the previous days. The black dotted (solid) line represents the average of TROPOMI AOD retrievals assuming  $n_r=1.47$  ( $n_r=1.39$ ) for pixels affected by Hunga aerosols that pass within 10 km of the Lucinda site. We adjusted TROPOMI retrieved AODs at 312nm to the AERONET measured AOD<sub>412</sub> using theoretical Hunga aerosol extinction spectral dependence shown in panel (b).

Panel (b) The red squares show the average spectral dependence of the AERONET AOD measurements during Hunga plume overpass at Lucinda shown in panel (a) and normalized to AOD<sub>412</sub> at 412nm. The  $3 \times$  standard deviation of the ratios AOD/AOD<sub>412</sub> is shown as a vertical bar ( $\pm 3\sigma$ ). The black solid (dotted) curve shows the theoretical Extinction ratio from Mie calculations assuming  $n_r=1.39$  ( $n_r=1.47$ ) and effective radius  $r_{eff} \sim 0.2 \mu m$ . The blue curves show similar extinction ratios using a larger  $r_{eff} \sim 0.4 \mu m$  retrieved in March 2022 by the solar occultation SAGE-III instrument aboard the International Space Station (Duchamp et al., 2023). It is clear that TROPOMI retrieval assumption of  $r_{eff} \sim 0.2 \mu m$  is consistent with the AERONET spectral AOD measurements during Hunga plume overpass on January 17 2022.

506 We estimated AOD retrieval uncertainties  $\varepsilon_{AOD}$  theoretically using different approaches: (1) using error estimation by the  
 507 Hunga retrieval algorithm diagnostic and comparing retrievals using low and high limits of  $n_r=1.39$  and 1.47 as shown in Fig.  
 508 10, and (2) comparing AOD retrievals for each Hunga pixel using short (289–296nm) and extended (289–310nm) spectral  
 509 fitting windows (see Fig. 3). We note the following:

510 (1) Retrieval  $\varepsilon_{AOD}$  uncertainties were initially based on TROPOMI radiance measurement noise (SNR) but were later refined  
 511 incorporating additional contributions derived from chi-square diagnostics accounting for discrepancies between  
 512 measured and simulated radiance ratios (see Section 3.3). Figure 10 shows the normalized probability density distribution  
 513 of the updated  $\varepsilon_{AOD}$  for all pixel retrievals in Hunga plume; this distribution has a long non-Gaussian tail; therefore, we  
 514 use the median and the interquartile range (IQR; 25th–75th percentile) statistics rather than the mean and the standard  
 515 deviation to describe an overall AOD uncertainty. The relative  $\varepsilon_{AOD}$  greatly increases for small AODs. When restricted  
 516 to cases with AOD >0.2, the median  $\varepsilon_{AOD} \sim 0.06$  and the corresponding IQRs are 0.02(0.03)–0.13 for for both  $n_r$  cases  
 517 (Fig. 10). Then normalizing to the retrieved AOD, this median absolute error corresponds to a median percentage error  
 518 of  $\sim 15\%$ .



**Figure 10: Normalized probability density function of retrieved Hunga  $\epsilon_{AOD}$  for the Hunga Plume on January 17, 2022. Results are shown for two different refractive index values:  $n_r = 1.47$  (red) and  $n_r = 1.39$  (blue). The number of valid retrievals with AOD  $> 0.2$  (N) and corresponding median and interquartile range (IQR; 25th–75th percentile) are indicated in the legend.**

519 (2) To estimate the upper limit of the  $\epsilon_{AOD}$ , we repeated TROPOMI Hunga retrievals using the extended spectral fitting  
 520 window (289–310 nm) (see Fig.3) and assuming upper limit of  $n_r = 1.47$ . With this long fitting window, we obtained AOD  
 521 values  $\sim 16\%$  lower than those obtained with the ‘short’ window. This reduction is possibly due to increased sensitivity to  
 522 tropospheric clouds and uncertainties in assumed gas-phase absorbers such as  $O_3$  and  $SO_2$ . These comparisons indicate  
 523 the importance of varying the spectral fitting window to estimate the upper limit of uncertainty of our Hunga aerosol  
 524 retrievals. On the other hand, using an extended spectral fitting window would permit retrieval of additional aerosol  
 525 parameters (*e.g.*, effective radius) or gases (*e.g.*,  $O_3$ ,  $SO_2$ ), but would require a more complex forward RT model (*e.g.*,  
 526 including tropospheric cloud correction).

527

528 Furthermore, to estimate potential instrument specific biases we carried out an inter-sensor comparison against the NOAA-20  
 529 OMPS Nadir Profiler (NP) based Hunga retrieval; this was conducted using the same ‘short’ spectral fitting window (289–296  
 530 nm) and assimilated  $O_3$  profiles (see Appendix E). The retrieved NOAA-20 OMPS-NP AOD values were approximately  $\sim 20\%$   
 531 higher than those from our TROPOMI retrievals collocated within six OMPS-NP pixels over Northeast Australia. Based on  
 532 these estimates, we adopt  $\pm 20\%$  as the total  $\epsilon_{AOD}$  percent uncertainty, considering both retrieval and instrument specific errors.

533

### 534 4.3 Aerosol Mass Retrievals

535 To convert the retrieved AOD to aerosol column mass  $m_{aer}$  [ $g/m^2$ ] we need to know particle mass density,  $\rho$ , effective radius  
 536  $r_{eff}$ , and extinction efficiency  $Q_{ext} = \frac{\langle E \rangle}{\langle G \rangle}$ , where  $\langle E \rangle$  and  $\langle G \rangle$  are average extinction and geometric cross-sections  
 537 (Krotkov et al., 1999ab; Duchamp et al., 2023; Sellitto et al., 2024):

538

539

$$m_{aer} = \frac{4 \rho r_{eff}}{3 Q_{ext}} AOD \quad (4.1)$$

540

541

542

543

544

545

546

547

548

549

550

We assume that the AERONET-retrieved fine-mode effective radius  $r_{eff} \sim 0.22 \mu\text{m}$  at Lucinda (Fig. 9b) is representative of the whole Hunga plume. To compare with the satellite infrared IASI retrievals, we assume mass density of  $\rho = 1.75 \text{ g cm}^{-3}$  (Sellitto et al., 2024). This density corresponds to a high sulfuric acid mass fraction  $w = 0.765$  at Hunga temperature  $T = 233\text{K}$  (Myhre et al., 1998) and a high value of  $n_r = 1.47$  at  $\sim 300\text{nm}$  (Beyer et al., 1996). These values are used in Eq. (4.1) to produce the spatial distribution of Hunga column aerosol mass  $m_{aer}$  shown in Fig. 11. The column mass spatial distribution has similar features to those in the AOD map (Fig. 8a). Using a BUUV radiance ratio filter at 296 nm ( $\text{CSI} > 1.1$ ) to define the plume, we estimate a total plume area  $A_{total} \sim 4 \times 10^6 \text{ km}^2$ , and a corresponding total wet aerosol mass ( $M_{aer} = 0.47 \text{ Tg}$ ), where “wet” denotes aqueous sulfuric acid solution droplets including water uptake at Hunga temperature  $T \sim 235\text{K}$  (Fig. 6) and high relative humidity  $\sim 60\%$  (see Appendix F). An  $m_{aer}$  up to  $\sim 0.8 \text{ g/m}^2$  was found over the densest part of the plume over the Coral Sea, as discussed in Section 4.2, given that the aerosol column mass values are proportional to the AOD. Over Northeast Australia,  $m_{aer}$  increased in value to  $\sim 0.5 \text{ g/m}^2$ , then decreased to  $m_{aer} \sim 0.05 \text{ g/m}^2$  over the northwestern part of Australia.

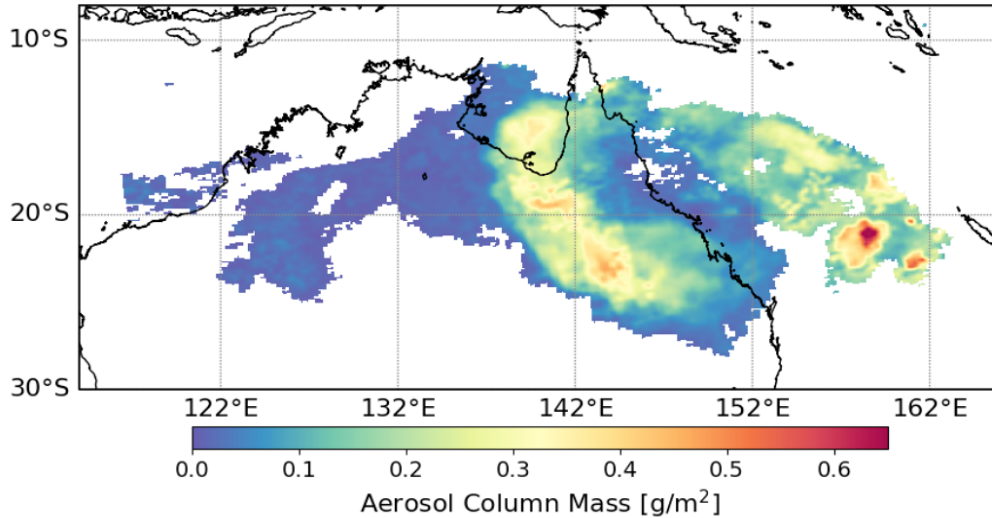


**Figure 11: Hunga aerosol column mass on January 17, 2022, assuming aqueous acid solution mass fraction 0.765, corresponding density  $\rho \sim 1.75 \text{ g/cm}^3$  (Myhre et al., 1998), refractive index,  $n_r = 1.47$  (Beyer et al., 1996), and an AERONET retrieved fine-mode effective radius  $r_{eff} \sim 0.22 \mu\text{m}$ .**

551

552

553

554

555

Both  $\rho$  and  $n_r$  are linked to the assumed sulfuric acid ( $\text{H}_2\text{SO}_4$ ) mass fraction ( $w$ ) in the aerosol solution droplets. Higher sulfuric acid content results in both higher  $n_r$  and  $\rho$ , and vice versa. To quantify the range of the total wet aerosol mass  $M_{aer}$ , we compared the retrieved  $m_{aer}$  using two limiting  $(n_r, \rho)$  pairs:

- for  $n_r = 1.47$  and  $\rho = 1.75 \text{ g/cm}^3$  ( $w_{max} = 0.765$ ), the integrated total wet aerosol mass  $M_{aer}$  is  $\sim 0.47 \text{ Tg}$ .
- for  $n_r = 1.39$  and  $\rho = 1.25 \text{ g/cm}^3$  ( $w_{min} = 0.291$ ), the integrated total wet aerosol mass  $M_{aer}$  is  $\sim 0.50 \text{ Tg}$ .

556 These results for  $M_{aer}$  are close; the increase in AOD and opposite decrease  $Q_{ext} = \frac{\langle E \rangle}{\langle G \rangle}$  values are responsible when going  
 557 from  $n_r = 1.47$  to  $n_r = 1.39$  in Eq. (4.1). They represent the lower and upper bounds of the retrieved wet aerosol mass, reflecting  
 558 the impact of microphysical assumptions on the retrieval. We provide a representative estimate of the total wet aerosol mass  
 559  $\sim 0.5 \pm 0.05$  Tg; this  $\sim 10\%$  uncertainty includes the AOD retrieval uncertainties discussed in Section 4.2.

560

#### 561 4.4 Estimate of Hunga sulfate ( $\text{H}_2\text{SO}_4$ ) mass fraction and $\text{H}_2\text{SO}_4/\text{H}_2\text{O}$ solution density

562 The wet aerosol mass  $M_{aer}$  retrieved in our study remains nearly constant ( $\sim 0.5 \pm 0.05$  Tg) for a broad range of assumed sulfuric  
 563 acid ( $\text{H}_2\text{SO}_4/\text{H}_2\text{O}$ ) solution concentrations in Hunga aerosol droplets. Therefore, it is interesting to independently estimate the  
 564 spatially-averaged sulfate ( $\text{H}_2\text{SO}_4$ ) mass fraction  $w$  and  $\text{H}_2\text{SO}_4/\text{H}_2\text{O}$  solution density  $\rho$ . For this, we assume conservation of  
 565 the total Hunga stratospheric sulfur ( $S$ ) mass  $M_{S_0}$  initially emitted in the gas phase as  $\text{SO}_2$  and an exponential  $\text{SO}_2$  to sulfate  
 566 conversion rate with an e-folding time of  $\tau$ , to estimate the expected  $S$  mass in the aerosol phase  $M_{S,aer}$  at time  $t$  ( $\sim 2$  days)  
 567 after the main eruption on January 15:

568

$$569 M_{S,aer} = M_{S_0} [1 - e^{(-\frac{t}{\tau})}] \quad (4.2)$$

570

571 We use reported Hunga gaseous sulfur ( $S$ ) emissions on January 15:  $M_{S_0} \sim 0.21 - 0.24$  TgS (*i.e.*, half the  $\text{SO}_2$  mass produced  
 572 by January 15 eruption) and an e-folding time of  $\tau \approx 6$  days as reported in Carn et al. (2022) to calculate the expected  $S$  mass  
 573 converted to aerosols after  $\sim 47$  hours of transport to be  $M_{S,aer} \sim 0.061 - 0.068$  TgS and a gaseous  $S$  mass (in  $\text{SO}_2$ ) to be  $M_{S,gas}$   
 574  $M_{S,gas} \sim 0.15 - 0.17$  TgS. Within uncertainties, the latter estimate agrees with independent operational TROPOMI  
 575 stratospheric  $\text{SO}_2$  retrievals (Theys et al., 2017) integrated within the Hunga aerosol plume on January 17 ( $\sim 0.14$  TgS; CSI >  
 576 1.1). The average sulfate ( $\text{H}_2\text{SO}_4$ ) mass fraction  $w$  can be estimated from the ratio of the  $M_{S,aer}$  to the retrieved total wet  
 577 aerosol mass  $M_{aer} \sim 0.5$  Tg, by accounting for their molar weight ratio: ( $MW_S \sim 32$  g/mol) and  $\text{H}_2\text{SO}_4$  ( $MW_{\text{H}_2\text{SO}_4} \sim 98$  g/mol):

578

$$579 w = \frac{M_{S,aer}}{M_{aer}} \frac{MW_{\text{H}_2\text{SO}_4}}{MW_S} \quad (4.3)$$

580

581 Applying this approach, we can estimate the Hunga sulfuric acid mass fraction to be  $w \sim 0.37 - 0.42$  with an average value of  
 582  $w \sim 0.4$  and an  $\text{H}_2\text{SO}_4/\text{H}_2\text{O}$  solution density estimated based on laboratory measurements of Myhre et al. (1998) at Hunga  
 583 plume temperature  $T \sim 235\text{K}$ :  $\rho \sim 1.34$  g/cm<sup>3</sup>. These new estimates based on Hunga stratospheric  $S$  mass balance are consistent  
 584 with the physics-based sulfate ( $\text{H}_2\text{SO}_4$ ) weight percent (wt%) simulation of Hunga aerosols using the NASA Goddard Earth  
 585 Observing System Chemistry Climate Model (GEOS CCM) with the Community Aerosol and Radiation Model for

586 Atmospheres (CARMA) similar to Case et al. (2023):  $\text{H}_2\text{SO}_4$  ~40-60 wt% (*i.e.*,  $w \sim 0.4$  to 0.6) and  $\rho \sim 1.3\text{--}1.4 \text{ g/cm}^3$  (see  
587 Appendix F).

588

#### 589 **4.5 Comparison with Infrared $\text{SO}_2$ Measurements**

590

591 Sellitto et al. (2024) reported retrievals of  $\text{SO}_2$  and sulfate aerosol mass in the Hunga plume based on mid-IR IASI  
592 measurements. Their study noted that  $\text{SO}_2$  and sulfate aerosol have overlapping spectral signatures in the IR, which can lead  
593 to large uncertainties in the co-retrieval of these species in volcanic plumes; however, the potential impact of collocated water  
594 vapor on the IR retrievals was not addressed. In their paper, the equation used to derive sulfate mass from IASI measurements  
595 of mid-IR AOD is identical to that used here (Eq. 4.1) but is based on the measured mid-IR AOD and average extinction  
596 efficiency ( $Q_{ext}$ ) calculated at mid-IR wavelengths ( $\sim 8.5 \mu\text{m}$ ). Sellitto et al. (2024) also assumed a sulfate aerosol mass density  
597 of  $\rho = 1.75 \text{ g cm}^{-3}$  which corresponds to the upper limit of the sulfuric solution concentration  $w = 0.765$  at temperature  $T =$   
598  $233\text{K}$  (Myhre et al., 1998). Additional uncertainties arise from the range of possible particle size distributions ( $r_{eff} \sim 0.25\text{--}0.45$   
599  $\mu\text{m}$ ) in the Hunga aerosol plume (Boichu et al., 2023; Duchamp et al., 2023).

600

601 These authors report a maximum Hunga sulfate aerosol mass loading of  $1.6 \pm 0.5 \text{ Tg}$ , but the peak loading was measured later  
602 in the year (August-September 2022). On January 17, 2022, the IASI-derived sulfate aerosol mass reported in Sellitto et al.  
603 (2024) is  $\sim 0.2 \text{ Tg}$ , with a large uncertainty (estimates range up to  $\sim 0.8 \text{ Tg}$ ). Our BUV-based wet aerosol mass of  $M_{aer} \sim 0.5 \text{ Tg}$   
604 is thus broadly consistent with these IR retrievals, given the uncertainties on the assumed particle size distribution. In contrast,  
605 a larger discrepancy is apparent in the  $\text{SO}_2$  retrievals: on January 17, the IASI-based  $\text{SO}_2$  mass is  $\sim 0.75 \text{ Tg}$  (range:  $\sim 0.4\text{--}1.1$   
606  $\text{Tg}$ ), compared to a total BUV  $\text{SO}_2$  mass of  $\sim 0.4 \text{ Tg}$  (note that this is the total retrieved  $\text{SO}_2$  mass on January 17, not the  $\text{SO}_2$   
607 collocated with the Hunga aerosol plume discussed in section 4.4). Furthermore, the IASI-based  $\text{SO}_2$  mass reached a maximum  
608 of  $\sim 1 \text{ Tg}$  (range:  $\sim 0.7\text{--}1.2 \text{ Tg}$ ) on January 19, 2022 (Sellitto et al., 2024), whereas the BUV  $\text{SO}_2$  mass was observed to decrease  
609 after January 17 (e.g., Carn et al., 2022).

610

611 Sadeghi et al. (2025) also retrieved Hunga  $\text{SO}_2$  mass using CrIS IR measurements in combination with the VOLCAT  
612 (VOLcanic Cloud Analysis Toolkit) framework. This work employed IR retrievals from the NASA-NOAA's Joint Polar  
613 Satellite System (JPSS) satellites and HYSPLIT-based trajectory analysis to assess  $\text{SO}_2$  transport and decay patterns. On  
614 January 16, 2022, Sadeghi et al. (2025) reported a CrIS-derived  $\text{SO}_2$  mass of  $\sim 0.4 \text{ Tg}$ , which is consistent with the BUV  $\text{SO}_2$   
615 mass reported in Carn et al. (2022).

616

617 The reasons for these discrepancies remain unclear. It is possible that the BUV operational  $\text{SO}_2$  measurements were more  
618 strongly impacted by the presence of optically thick aerosol; we also propose that the impact of Hunga water vapor on the IR  
619  $\text{SO}_2$  and sulfate mass retrievals may also merit further consideration.

620

## 621 **5. Summary and Conclusions**

622 The January 15, 2022 eruption of the submarine Hunga volcano was a unique volcanic event in the ~50 years since the  
623 beginning of the satellite remote sensing era. This powerful eruption was the largest since Pinatubo in 1991, but unlike the  
624 SO<sub>2</sub>-rich Pinatubo emissions, Hunga injected a volcanic plume dominated by water vapor, with relatively low SO<sub>2</sub> content, to  
625 altitudes as high as the lower mesosphere. Although the Hunga eruption has been studied intensively from a number of remote  
626 sensing perspectives, in this work we have presented a novel retrieval of aerosol mass and layer height using BUUV  
627 measurements from the S5P/TROPOMI instrument on January 17, 2022. These unique BUUV retrievals allow us to detect and  
628 characterize the mid-stratospheric Hunga aerosol plume that moved across the Southwest Pacific and Australia about 47 hours  
629 after the January 15 eruption. This study demonstrates for the first time that BUUV radiance measurements can be used to  
630 retrieve simultaneously mid-stratospheric non-absorbing volcanic aerosol optical depth (AOD) and the aerosol peak height  
631 ( $Z_p$ ) above the ozone density peak ~25 km, following a major volcanic eruption.

632

633 Our algorithm simultaneously retrieves AOD and  $Z_p$  using BUUV radiance ratios (TROPOMI measurements in the presence of  
634 the Hunga aerosol plume divided by background aerosol-free measurements from a preceding orbit) in the 289–296nm spectral  
635 fitting window insensitive to tropospheric aerosols and clouds. To identify Hunga aerosol plumes, we empirically determined  
636 the threshold of the ratioed BUUV radiances at 296 nm (CSI, cloud screening index), restricting retrievals to TROPOMI pixels  
637 with CSI>1.1. Our work also provides an explanation for the observed anomalies in total ozone column (TOC) BUUV retrievals  
638 in the presence of the Hunga aerosol plume, when enhanced aerosol scattering increases BUUV radiances, leading to erroneously  
639 low anomalies in operational TOC retrievals. In this study, the assimilated Microwave Limb Sounder (MLS) O<sub>3</sub> profile data  
640 (from reprocessed M2-SCREAM reanalysis excluding the anomalous BUUV TOC retrievals in the assimilation) were used to  
641 properly account for strong ozone absorption effects. For the Hunga aerosol retrieval, Mie calculations were performed in the  
642 UV range, based on a wide range of refractive indices of H<sub>2</sub>SO<sub>4</sub>/H<sub>2</sub>O solutions at stratospheric temperatures. We use  
643 AERONET inversions of the aerosol size distribution to constrain effective radius  $r_{eff} \sim 0.22 \mu m$  and the width  $S_g = 1.545$  of  
644 the Hunga particle size distribution. We have developed a new forward-modeling tool based on the VLIDORT vector radiative  
645 transfer code, with the retrieval algorithm state vector comprising only two aerosol parameters: the AOD at 312 nm and  $Z_p$ .

646 Our aerosol retrievals are generally consistent with concurrent satellite-based retrievals using space lidar (CALIOP), Multi-  
647 angle Imaging Spectro-Radiometer (MISR), NOAA-20 OMPS Nadir Profiler (OMPS-NP) and ground-based AERONET AOD  
648 measurements using trajectory modeling. Additionally, trajectory modeling showed that air parcels back-propagated from  
649 TROPOMI retrievals were consistent with the stratospheric wind and transport pathways of the Hunga plume.

650

651 We used the retrieved AOD to estimate a Hunga total wet aerosol mass (sulfuric acid (H<sub>2</sub>SO<sub>4</sub>) solution droplets, including  
652 water uptake) to be  $\sim 0.5 \pm 0.05 Tg$  on January 17, just two days after the main eruption. This mass estimate is consistent with

653 our previous BUUV retrievals of Hunga sulfur dioxide (SO<sub>2</sub>) emissions ( $\sim 0.4\text{--}0.5 \text{ TgSO}_2$  from January 15 eruption) and rapid  
 654 conversion of SO<sub>2</sub> to sulfate aerosol (e-folding time  $\sim 6$  days).

655

656 Based on our new aerosol and operational SO<sub>2</sub> BUUV retrievals we estimated the sulfate (H<sub>2</sub>SO<sub>4</sub>) mass fraction  $w \sim 0.4$  in Hunga  
 657 solution droplets and H<sub>2</sub>SO<sub>4</sub>/H<sub>2</sub>O solution density:  $\rho \sim 1.34 \text{ g/cm}^3$ . These parameters represent a significant deviation from  
 658 the typical stratospheric background sulfate aerosol (Junge layer), which is typically characterized by values of  $w \sim 0.75$   
 659 and  $\rho \sim 1.7 \text{ g/cm}^3$ . These reference values were originally derived by Toon & Pollack (1973) and are backed up by decades of  
 660 observations of the lower stratosphere during both quiescent and volcanically impacted periods. The new values, inferred in  
 661 Section 4.4 from BUUV satellite observations and supported by microphysical modeling, are a result of the uniquely water-rich  
 662 conditions in the early Hunga plume. Relative humidity in the plume, as modeled by NASA Goddard Earth Observing System  
 663 Chemistry-Climate Model with the Community Aerosol and Radiation Model for Atmospheres (CARMA), reached values as  
 664 high as 60%, in sharp contrast to background levels of  $\sim 1\%$ . These findings are unique in the long observational record of the  
 665 stratosphere; similar relative humidities only otherwise occur in overshooting clouds or cold winter hemisphere vortices.

666

## 667 **Appendix A. Aerosol Plume Parameterization**

668 The treatment here follows that in (Spurr and Christi, 2014). We use the same pseudo-Gaussian plume parameterization scheme  
 669 for aerosols and for the other trace gases (SO<sub>2</sub>, O<sub>3</sub>); the exposition here is given just for aerosols but applies equally to the two  
 670 trace species. The aerosol plume is characterized by three parameters  $\{A_0, z_p, h_w\}$ :  $A_0$  is the plume total optical depth at a fixed  
 671 reference wavelength  $\lambda_{ref}$  (312 nm),  $z_p$  is the plume peak height in [km], and  $h_w$  is the HWHM in [km] of the plume  
 672 distribution. We retrieve the first two of these parameters; the state vector is  $x = \{A_0, z_p\}$ . The pseudo-Gaussian plume is the  
 673 aerosol optical thickness profile at 312 nm, given by:

$$674 \quad \tau(z) = \Omega \frac{\exp[-f(z-z_p)]}{[1+\exp[-f(z-z_p)]]^2}. \quad (\text{A2.1})$$

675 Here,  $z$  is the altitude,  $z_p$  is the peak height (“PKH”),  $\Omega$  is a normalization constant related to total stratospheric aerosol optical  
 676 thickness (“AOD”)  $A_0$ , and  $f$  is an exponential constant related to the HWHM parameter  $h_w$  through  $f h_w = \ln[3 + 2\sqrt{2}]$ .

677 At peak height  $z = z_p$ , the loading is  $\tau(z_p) = \frac{1}{4}\Omega$ .

678 We assume that the plume lies between two limiting heights  $z_b$  and  $z_t$ . Integrating the profile between these limits yields the  
 679 total AOD:

$$680 \quad A_0 = \int_{z_b}^{z_t} \tau(z) dz = \Omega \Gamma; \quad \Gamma = \frac{(Y_b - Y_t)}{(1+Y_b)(1+Y_t)}; \quad (\text{A2.2})$$

$$681 \quad Y_b = \exp \exp[-f(z_b - z_p)]; \quad Y_t = \exp \exp[-f(z_t - z_p)]. \quad (\text{A2.3})$$

682 For a discretization of the atmosphere into vertical layers  $\{z_n\}, n = 0, 1, \dots, N_L$ , where  $N_L$  is the total number of layers, the  
 683 loading profile will be given by:

$$684 \quad L_n = \int_{z_n}^{z_{n-1}} \tau(z) dz = \frac{A_0}{\Gamma} \Gamma_n; \quad (A2.4)$$

$$685 \quad \Gamma_n = \frac{(Y_n - Y_{n-1})}{(1+Y_n)(1+Y_{n-1})}; \quad Y_n = \exp[-f(z_n - z_p)]. \quad (A2.5)$$

686 Here we have used Eq. (A2.2) to show that each layer amount  $L_n$  is directly proportional to  $A_0$ . The forward model radiative  
 687 transfer calculation using VLIDORT requires Jacobians with respect to  $A_0$  and  $z_p$ , plus  $h_w$  if the latter is to be included in the  
 688 retrieval or is to be considered as a model parameter error in the retrieval. We require partial derivatives of the loading profile  
 689 with respect to these parameters. Explicit differentiation of Eq. (A2.4) gives:

$$691 \quad \frac{\partial L_n}{\partial A_0} = \frac{\Gamma_n}{\Gamma}; \quad \frac{\partial L_n}{\partial z_p} = \frac{1}{\Gamma} \cdot \left[ \frac{\partial \Gamma_n}{\partial z_p} - L_n \frac{\partial \Gamma}{\partial z_p} \right]; \quad \frac{\partial L_n}{\partial h_w} = \frac{1}{\Gamma} \cdot \left[ \frac{\partial \Gamma_n}{\partial h_w} - L_n \frac{\partial \Gamma}{\partial h_w} \right]. \quad (A2.6)$$

692  
 693 The  $A_0$  derivative is trivial. Derivatives with respect to  $z_p$  are harder to establish; after some algebra, we find the auxiliary  
 694 derivatives of  $\Gamma$  and  $\Gamma_n$  through:

$$695 \quad \frac{\partial \Gamma_n}{\partial z_p} = f \Gamma_n \frac{(1 - Y_n Y_{n-1})}{(1 + Y_n)(1 + Y_{n-1})}; \quad \frac{\partial \Gamma}{\partial z_p} = f \Gamma \frac{(1 - Y_b Y_t)}{(1 + Y_b)(1 + Y_t)}. \quad (A2.7)$$

696  
 697 Similarly, the auxiliary derivative  $\Gamma_n$  with respect to  $h_w$  is given by:

$$698 \quad \frac{\partial \Gamma_n}{\partial h_w} = -\frac{C}{f^2} \Gamma_n \left[ z_p - \frac{(z_n Y_n - z_{n-1} Y_{n-1})}{(Y_n - Y_{n-1})} + \frac{(z_n - z_p) Y_n}{(1 + Y_n)} + \frac{(z_{n-1} - z_p) Y_{n-1}}{(1 + Y_{n-1})} \right]. \quad (A2.8)$$

699  
 700 A similar expression holds for the derivative of  $\Gamma$  with respect to  $h_w$ , but with  $Y_b$  and  $z_b$  replacing  $Y_n$  and  $z_n$ , and  $Y_t$  and  $z_t$   
 701 replacing with  $Y_{n-1}$  and  $z_{n-1}$ . In Eq. (A2.8), the constant  $C = \ln[3 + \sqrt{8}]$ .

702 Figure A1 (top panel) illustrates three typical pseudo-Gaussian plumes, with total AOD  $A_0 = 1.81$ , peak height  $z_p = 31.5$  km  
 703 and three different values of  $h_w$  as indicated. The lower panels show the partial derivatives with respect to  $A_0$  and  $z_p$ .

704 Treatment of the SO<sub>2</sub> trace gas profiles is similar. Plume parameters are the total column  $\Omega_{SO_2}$  in [DU], and the aerosol  
 705 parameters  $z_p$  and  $h_w$ , when the plumes are positioned together and have the same shape. In this case, derivatives of the SO<sub>2</sub>  
 706 plume profile with respect to  $z_p$  and  $h_w$  will then have exactly the same form as the expressions in Eqns. (A2.6) to (A2.8).

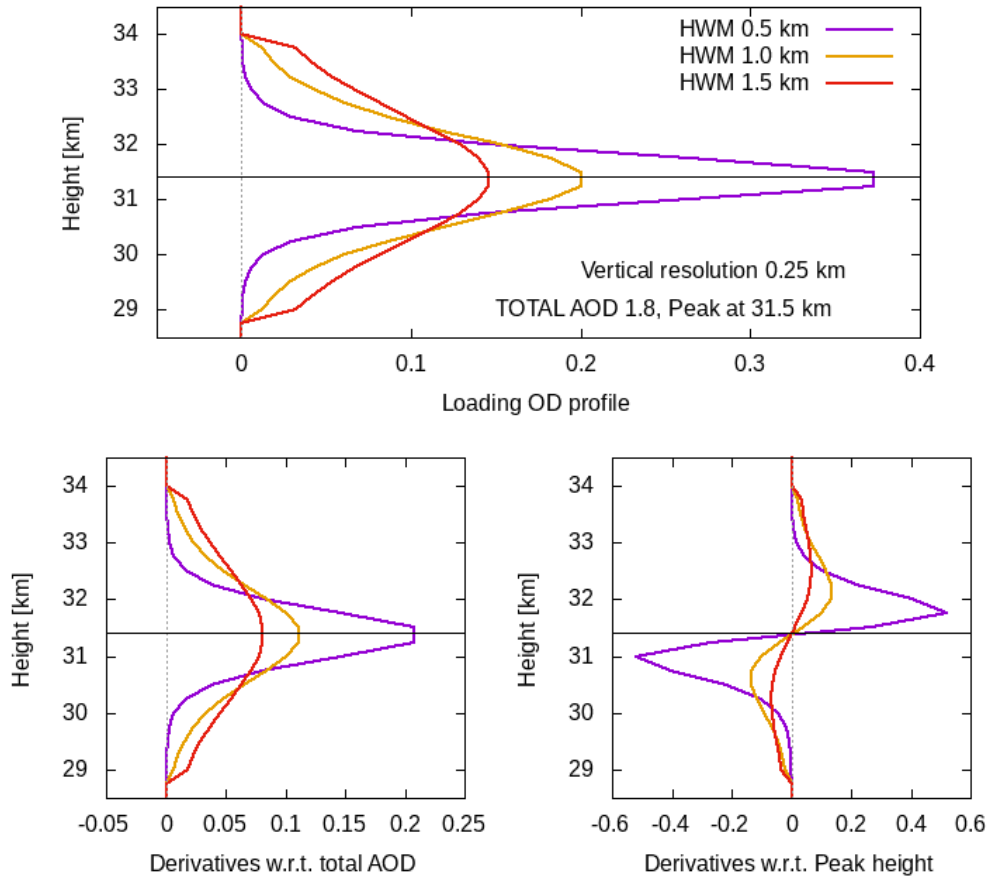


**Figure A1: (Upper panel) Pseudo-Gaussian aerosol plume profiles over the 28–35 km height range, for three different HWHM values as indicated. (Lower panels) Profile derivatives with respect to AOD and peak height.**

## 707 Appendix B. VLIDORT and the Forward Model

708 For radiance simulations, it is necessary to construct in input set of total optical properties (optical thickness values, single-  
 709 scattering albedos, spherical-function expansion coefficients, scattering matrices) for VLIDORT. In addition, for calculations  
 710 of associated Jacobians with respect to aerosol retrieval parameters, VLIDORT requires an additional set of linearized total  
 711 optical property inputs. Determination of VLIDORT optical property inputs is discussed in this Appendix. VLIDORT is a  
 712 discrete-ordinate polarized radiative transfer (RT) model in wide use in the remote sensing community. Single scattering in  
 713 VLIDORT is treated accurately for line-of-sight and solar paths allowing for the Earth’s curvature, while the multiple-scatter  
 714 field is determined through plane-parallel scattering along with the pseudo-spherical approximation (solar beam attenuation  
 715 for a curved atmosphere). The great advantage using VLIDORT lies in its ability to return not just the backscattered Stokes-  
 716 vector radiation field, but also analytically-derived Jacobians of this field with respect to any atmospheric or surface property.  
 717

718 To cover all possible retrieval trials discussed in this work and planned sequel papers, we require VLIDORT to calculate  
 719 Jacobians with respect to the three aerosol parameters  $\{A_0, z_p, h_w\}$ , the single SO<sub>2</sub> parameter  $\{\Omega_{SO_2}\}$  and the three O<sub>3</sub> parameters  
 720  $\{\Omega_{O_3}, z_{p,O_3}, h_{w,O_3}\}$ .

721 In VLIDORT, the atmosphere is taken as a series of optically uniform layers. Without loss of generality, the standard set of  
 722 input optical properties (IOPs) is  $\{\Delta_n, \omega_n, B_{nl}\}$ ,  $n = 1, \dots, N_L$ , where  $\Delta_n$  is the layer optical depth for extinction in layer  $n$ ,  $\omega_n$   
 723 the total single scattering albedo in that layer, and  $B_{nl}$  is a 4x4 matrix of spherical-function expansion coefficients that are used  
 724 to develop the total scattering and phase matrices. [Scattering matrices can be specified in advance for the single-scattering  
 725 calculations, as an alternative to developing them from sets of expansion coefficients]. For Jacobians, VLIDORT also requires  
 726 the set of *linearized* IOPs  $\{V_{nq}, U_{nq}, Z_{nlq}\}$ ,  $n = 1, \dots, N_L$  defined as the double-normalized partial derivatives of the IOPs with  
 727 respect to Jacobian parameter  $\xi_q$ . In other words:

$$728 \quad V_{nq} = \frac{\xi_q}{\Delta_n} \frac{\partial \Delta_n}{\partial \xi_q}; \quad U_{nq} = \frac{\xi_q}{\omega_n} \frac{\partial \omega_n}{\partial \xi_q}; \quad Z_{nlq} = \frac{\xi_q}{B_{nl}} \frac{\partial B_{nl}}{\partial \xi_q}. \quad (B2.1)$$

729 Here, we determine these IOPs and associated parameter derivatives for the present application.

730

731 If the trace gas absorption optical thickness is  $G_n(\lambda)$  in layer  $n$ , the Rayleigh scattering optical thickness  $R_n(\lambda)$ , and the aerosol  
 732 extinction optical thickness  $E_n(\lambda)$  at wavelength  $\lambda$ , then the IOPs in that layer are:

$$733 \quad \Delta_n(\lambda) = G_n(\lambda) + R_n(\lambda) + E_n(\lambda); \quad (B2.2a)$$

$$734 \quad \omega_n(\lambda) = \frac{R_n(\lambda) + a(\lambda)E_n(\lambda)}{\Delta_n(\lambda)}; \quad (B2.2b)$$

$$735 \quad B_{nl}(\lambda) = \frac{R_n(\lambda)B_l^{(Ray)}(\lambda) + a(\lambda)E_n(\lambda)B_l^{(Aer)}(\lambda)}{R_n(\lambda) + a(\lambda)E_n(\lambda)}. \quad (B2.2c)$$

736 Here  $a(\lambda)$  is the aerosol single scatter albedo, with  $B_l^{(Ray)}$  and  $B_l^{(Aer)}$  the coefficient matrices for Rayleigh and aerosol  
 737 scattering respectively.

738 Now the aerosol optical thickness  $E_n(\lambda)$  is related to the aerosol loading profile  $\{L_n\}$  at reference wavelength  $\lambda_0$  through:

$$739 \quad E_n(\lambda) = r(\lambda)L_n = \frac{\epsilon(\lambda)}{\epsilon(\lambda_0)}L_n. \quad (B2.3)$$

740 Here,  $\epsilon(\lambda)$  is the coefficient for aerosol extinction at the wavelength of interest, with  $\epsilon(\lambda_0)$  the extinction coefficient at  
 741 reference wavelength  $\lambda_0$ , with  $r(\lambda)$  the ratio of these two quantities.

742

743 Similarly, the trace gas absorption term (with SO<sub>2</sub> included) is

$$744 \quad G_n(\lambda) = \sigma_{n,O_3}(\lambda)L_{n,O_3} + \sigma_{n,SO_2}(\lambda)L_{n,SO_2}; \quad (B2.4)$$

745 Here,  $\{L_{n,O_3}\}$  and  $\{L_{n,SO_2}\}$  are trace gas loading profiles, with absorption cross-sections denoted by  $\sigma_{n,O_3}(\lambda)$  and  $\sigma_{n,SO_2}(\lambda)$ .

746 Given the aerosol loading profile  $\{L_n\}$  and gas profiles  $\{L_{n,O_3}\}, \{L_{n,SO_2}\}$ , we are now in a position to derive the linearized  
 747 optical properties in Eq. (B2.1) through explicit chain-rule differentiation of the results In Eq. (B2.2)-B(2.4) with respect to  
 748 any of the three aerosol parameters  $\{A_0, z_p, h_w\}$ , the SO<sub>2</sub> parameter  $\{\Omega_{SO_2}\}$  or the three O<sub>3</sub> parameters  $\{\Omega_{O_3}, z_{p,O_3}, h_{w,O_3}\}$ .  
 749 Dealing first with the aerosol profile  $\{L_n\}$ , and using the symbol  $\xi$  to indicate any one of the parameters  $\{A_0, z_p, h_w\}$ , we find  
 750 that:

$$751 \quad \frac{\partial \Delta_n(\lambda)}{\partial \xi} = r(\lambda) \frac{\partial L_n}{\partial \xi}, \quad (B2.5a)$$

$$752 \quad \frac{\partial \omega_n(\lambda)}{\partial \xi} = r(\lambda) \frac{\partial L_n}{\partial \xi} \cdot \left[ \frac{a(\lambda) - \omega_n(\lambda)}{\Delta_n(\lambda)} \right], \quad (B2.5b)$$

$$753 \quad \frac{\partial B_{nl}(\lambda)}{\partial \xi} = a(\lambda) r(\lambda) \frac{\partial L_n}{\partial \xi} \cdot \left[ \frac{B_{nl}^{(Aer)}(\lambda) - B_{nl}(\lambda)}{R_n(\lambda) + a(\lambda) E_n(\lambda)} \right]. \quad (B2.5c)$$

754 Dealing next with the O<sub>3</sub> profile  $\{L_{n,O_3}\}$  and setting  $\xi_{O_3}$  to any of the three O<sub>3</sub> parameters  $\{\Omega_{O_3}, z_{p,O_3}, h_{w,O_3}\}$ , we have:

$$755 \quad \frac{\partial \Delta_n(\lambda)}{\partial \xi_{O_3}} = \sigma_{n,O_3}(\lambda) \frac{\partial L_{n,O_3}}{\partial \xi_{O_3}}, \quad (B2.6a)$$

$$756 \quad \frac{\partial \omega_n(\lambda)}{\partial \xi_{O_3}} = -\frac{\omega_n(\lambda)}{\Delta_n(\lambda)} \cdot \frac{\partial \Delta_n(\lambda)}{\partial \xi_{O_3}}, \quad (B2.6b)$$

$$757 \quad \frac{\partial B_{nl}(\lambda)}{\partial \xi_{O_3}} = 0. \quad (B2.6c)$$

758 Note that these ozone derivatives are only present for the parameterized part of the profile; outside this range they are zero.  
 759 The situation with SO<sub>2</sub> is a little more complicated. For the SO<sub>2</sub> loading parameter  $\Omega_{SO_2}$ , the derivatives are of the same form  
 760 as those in Eqn. (B2.6):

$$761 \quad \frac{\partial \Delta_n(\lambda)}{\partial \Omega_{SO_2}} = \sigma_{n,SO_2}(\lambda) \frac{\partial L_{n,SO_2}}{\partial \Omega_{SO_2}}; \quad \frac{\partial \omega_n(\lambda)}{\partial \Omega_{SO_2}} = -\frac{\omega_n(\lambda)}{\Delta_n(\lambda)} \cdot \frac{\partial \Delta_n(\lambda)}{\partial \Omega_{SO_2}}; \quad \frac{\partial B_{nl}(\lambda)}{\partial \Omega_{SO_2}} = 0. \quad (B2.7)$$

762 If the SO<sub>2</sub> plume is coincident with the aerosol plume, then there will be additional dependencies on the parameters  $\{z_p, h_w\}$ .  
 763 Thus we now have (in place of (B2.5)):

$$764 \quad \frac{\partial \Delta_n(\lambda)}{\partial z_p} = r(\lambda) \frac{\partial L_n}{\partial z_p} + \sigma_{n,SO_2}(\lambda) \frac{\partial L_{n,SO_2}}{\partial z_p}, \quad (B2.8a)$$

$$765 \quad \frac{\partial \omega_n(\lambda)}{\partial z_p} = \frac{1}{\Delta_n(\lambda)} \left[ a(\lambda) r(\lambda) \frac{\partial L_n}{\partial z_p} - \omega_n(\lambda) \frac{\partial \Delta_n(\lambda)}{\partial z_p} \right]; \quad (B2.8b)$$

$$766 \quad \frac{\partial B_{nl}(\lambda)}{\partial z_p} = a(\lambda) r(\lambda) \frac{\partial L_n}{\partial z_p} \cdot \left[ \frac{B_{nl}^{(Aer)}(\lambda) - B_{nl}(\lambda)}{R_n(\lambda) + a(\lambda) E_n(\lambda)} \right]. \quad (B2.8c)$$

767 This establishes the necessary optical inputs for VLIDORT to return simulated radiances and Jacobians for our retrieval trials.  
 768 More details on optical property setups for VLIDORT may be found in the review literature (Spurr and Christi, 2019).

## 769 Appendix C. Determination of CSI Threshold

770 To identify Hunga aerosol plume pixels and reduce interference with tropospheric clouds, we use a Cloud Screening Index  
 771 (CSI), which is defined as a TROPOMI radiance ratio at a specific wavelength below 300nm. The CSI wavelength and  
 772 threshold were determined empirically. Radiance-ratio maps were generated at 0.5 nm intervals between 280 nm and 330 nm

773 and examined (see Supplement S1). We found that short UV1 wavelengths fail to fully capture the Hunga plume, while longer  
 774 UV2 wavelengths are affected by tropospheric clouds more than by Hunga aerosols (Figures 2–4). Based on this analysis,  
 775 radiance ratios at 296, 297, and 298 nm were selected as candidates for the CSI representative wavelength, since they  
 776 minimized interference with tropospheric clouds while retaining good sensitivity to the Hunga volcanic aerosols. Figure C1  
 777 shows retrieved Hunga AOD maps filtered using the CSI at the candidate wavelengths (296, 297, and 298 nm) with CSI  
 778 thresholds set at 1.05 and 1.1. Areas marked with black circles indicate regions influenced by tropospheric clouds. The  
 779 threshold of 1.05 was found to be too low to effectively filter out tropospheric clouds at representative wavelengths. When the  
 780 threshold was increased to 1.1, filtering at 297 nm and 298 nm still left some tropospheric cloud pixels, whereas filtering at  
 781 296 nm screened out most tropospheric clouds and captured most of the Hunga aerosol plume pixels (see Figure 3). Therefore,  
 782 the radiance ratio at 296 nm was selected as the CSI wavelength, with the associated threshold set to be 1.1.  
 783

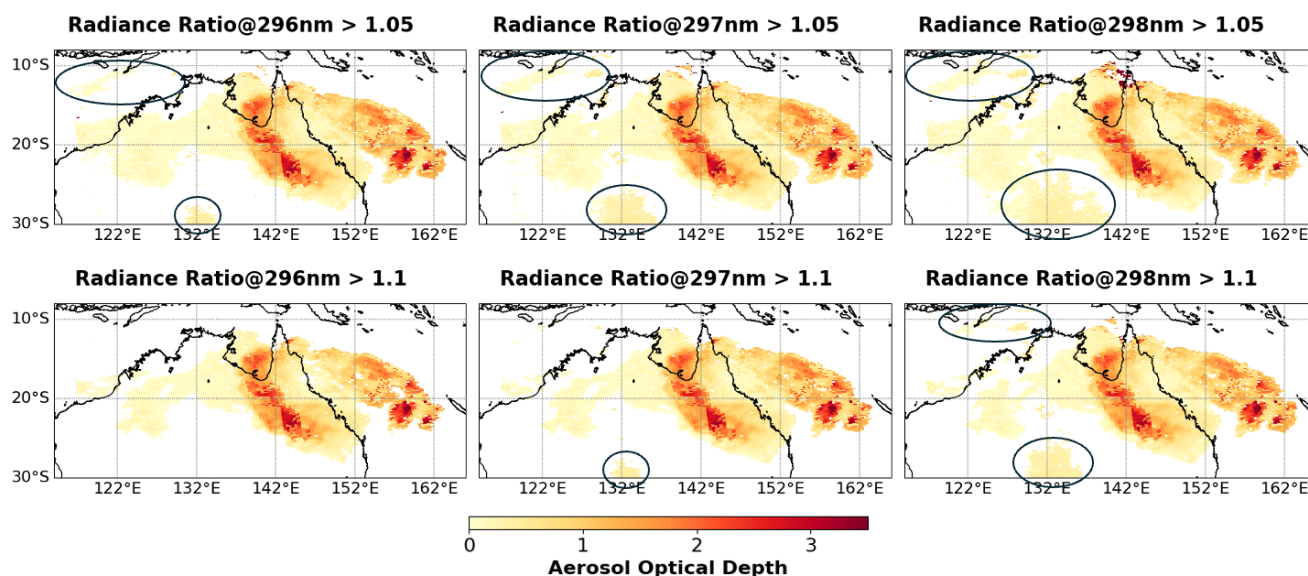


**Figure C1: Hunga-retrieved AOD maps generated by filtering pixels based on radiance-ratio thresholds (1.05 and 1.1) at three candidate CSI wavelengths of 296, 297, and 298 nm. Black circles indicate areas mainly influenced by tropospheric clouds.**

#### 784 **Appendix D. NASA Goddard Trajectory Calculation of Hunga Aerosol Transport**

785 The “ftraj” trajectory model from NASA’s Goddard Space Flight Center Atmospheric Chemistry and Dynamics Laboratory  
 786 uses a fourth-order Runge–Kutta integration scheme to track parcels isentropically, with optional diabatic adjustments  
 787 (Schoeberl and Sparling, 1995). The model is driven with winds at  $0.25^\circ$  horizontal resolution and spaced every 6 hours, from  
 788 the Goddard Earth Observing System (GEOS) forward-processing system produced by the NASA Global Modeling and  
 789 Assimilation Office (GMAO).

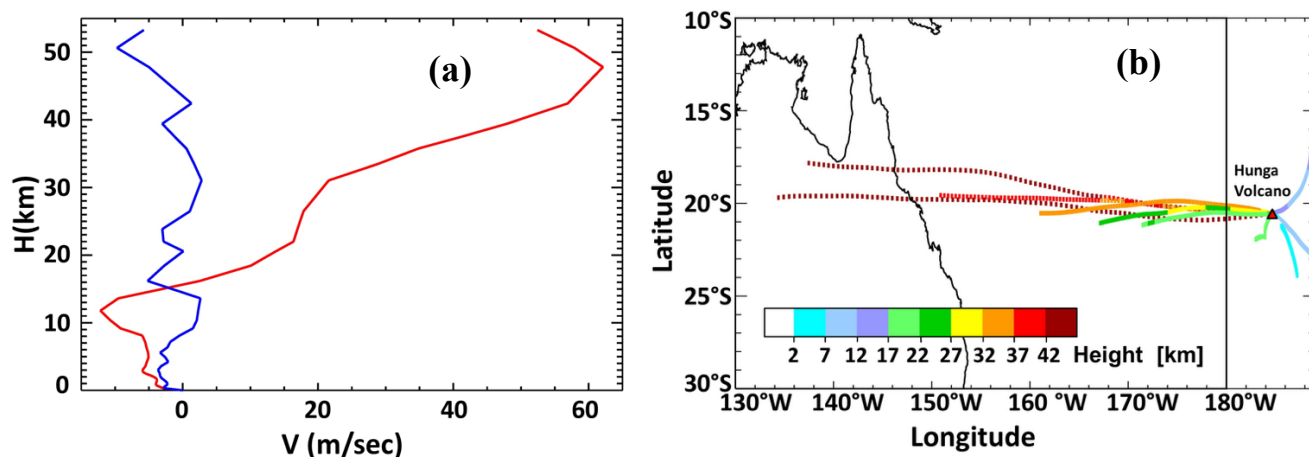


**Figure D1: (a) Wind vertical profile near the Hunga volcano at the time of the eruption. The blue curve shows the speed of the meridional wind, the red curve the speed of the zonal wind. Clearly the meridional wind is weak at all altitudes, while the easterly winds increase with altitude. (b) Forward trajectories of air parcels that start from a location directly above the Hunga volcano at different heights, followed through 24 hours using MERRA-2 reanalysis winds.**

790

791 Figure D1b shows several trajectories calculated using the “ftraj” model. Parcels are started from nadir locations above the  
 792 eruption point at different heights. In full accordance with the wind field, the tropospheric part of the volcanic plume at altitudes  
 793 less than 17 km slowly drifts eastward, while the stratospheric part at altitudes higher than 17 km quickly moves westward.

#### 794 **Appendix E. Hunga Aerosol Retrieval from NOAA-20 OMPS-NP measurements**

795 The NOAA-20 OMPS Nadir Profiler (OMPS-NP) provides backscattered ultraviolet (BUV) radiance spectra in the nadir  
 796 viewing direction with a higher SNR, but a lower spectral resolution (FWHM  $\sim 1$  nm) than correspondingly for TROPOMI in  
 797 the UV1 and UV2 spectral regions. Given the high SNR and spectral coverage of OMPS-NP, we conducted independent  
 798 retrievals of AOD and aerosol layer height ( $Z_p$ ) within the Hunga plume. Figure E1 shows (left) the radiance ratio map (CSI  
 799 at 296 nm) and (right) spectral radiance ratios along the Hunga plume orbit (o21577), referenced to a background orbit  
 800 (o21575) on January 17, 2022. The enhancements of radiance ratios are consistent with the TROPOMI radiance ratio patterns  
 801 presented in Fig. 1. The clear enhancement of OMPS-NP radiance ratios within the Hunga plume and the high SNR of OMPS-  
 802 NP indicate that OMPS-NP data are sensitive enough to retrieve AOD and  $Z_p$ . The same forward model inputs as described in  
 803 Section 3 (e.g., corrected ozone profiles from M2-SCREAM and aerosol microphysical properties) were used in the OMPS-  
 804 NP retrievals. Since spectral SNR values are required to construct the measurement and forward-model error covariance matrix  
 805  $S_e$  (as noted in Section 3.3) and considering the noteworthy stray light rejection characteristics of the OMPS-NP instrument,  
 806 the spectral SNR of OMPS-NP was assumed to be five times higher than the TROPOMI UV1 SNR.

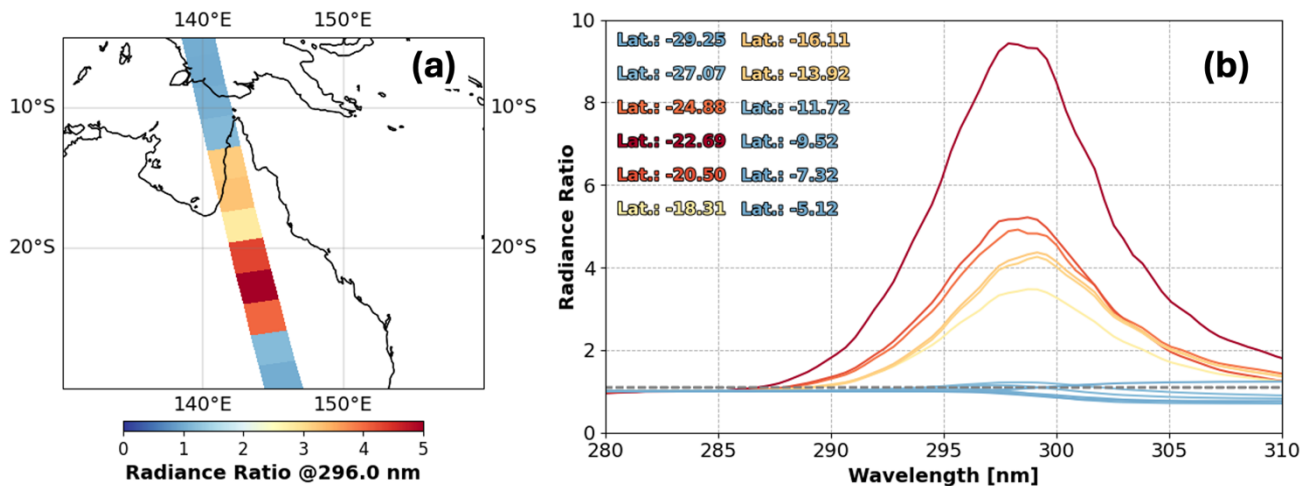


Figure E1: (Left) OMPS-NP CSI map (radiance ratio at 296 nm) for the plume orbit (o21575) on January 17, 2022. (Right) OMPS-NP spectral radiance ratios (280–310 nm) along the plume orbit (along-track: 35–46; Latitudes: 29.25°S to 5.12°S) on January 17, 2022. Same color scale is applied to both plots. Spectral radiance ratios were derived from the ratio between the plume orbit (o21577) and the background orbit (o21575).

807

808 Figure E2 shows the retrieved AOD and  $Z_p$  maps from OMPS-NP and TROPOMI along with their absolute and percentage  
 809 differences. Both retrievals were performed assuming  $n_r = 1.47$ . Smaller TROPOMI pixels were aggregated within OMPS-NP  
 810 pixels, and to ensure a reasonable comparison, we excluded cases where the number of TROPOMI Hunga pixels with CSI >  
 811 1.1 was less than 20% of the total number of collocated pixels. Retrieved AOD and  $Z_p$  values are compared in Table E1 for  
 812 OMPS-NP pixels 37 to 42. As shown in Fig. E2, the spatial distributions of  $Z_p$  and AOD from OMPS-NP and aggregated  
 813 TROPOMI pixels show good agreement. OMPS-NP  $Z_p$  values are slightly lower than those of TROPOMI with an absolute  
 814 difference (OMPS-NP minus TROPOMI) of  $0.25 \pm 0.15$  km, with an averaged absolute percentage difference of  $\sim 0.8\%$ ,  
 815 indicating excellent consistency in  $Z_p$  retrievals between the two sensors. However, OMPS-NP AOD values are approximately  
 816  $\sim 20\%$  higher than those from TROPOMI ( $0.24 \pm 0.17$ ). This result suggests that the higher SNR of OMPS-NP better capture  
 817 enhanced aerosol signals, while TROPOMI still retrieves  $Z_p$  values comparable to OMPS-NP.

818

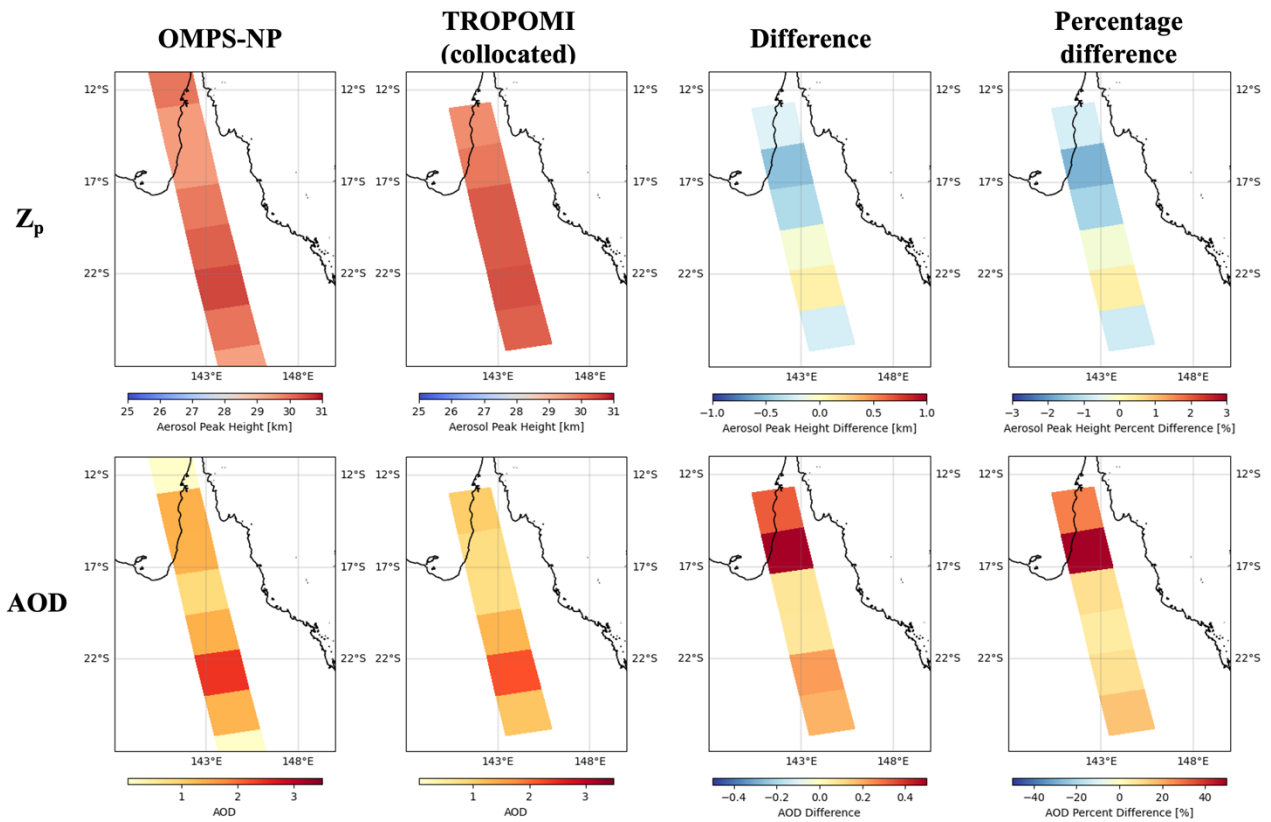


Figure E2: (Upper row) Aerosol peak height ( $Z_p$ ) maps retrieved from OMPS-NP and TROPOMI measurements assuming  $n_r = 1.47$ , along with absolute and percentage differences between the two retrievals. (Lower row) Same as upper panel, but for the AOD. TROPOMI  $Z_p$  and AOD values were collocated to match each OMPS-NP along-track location.

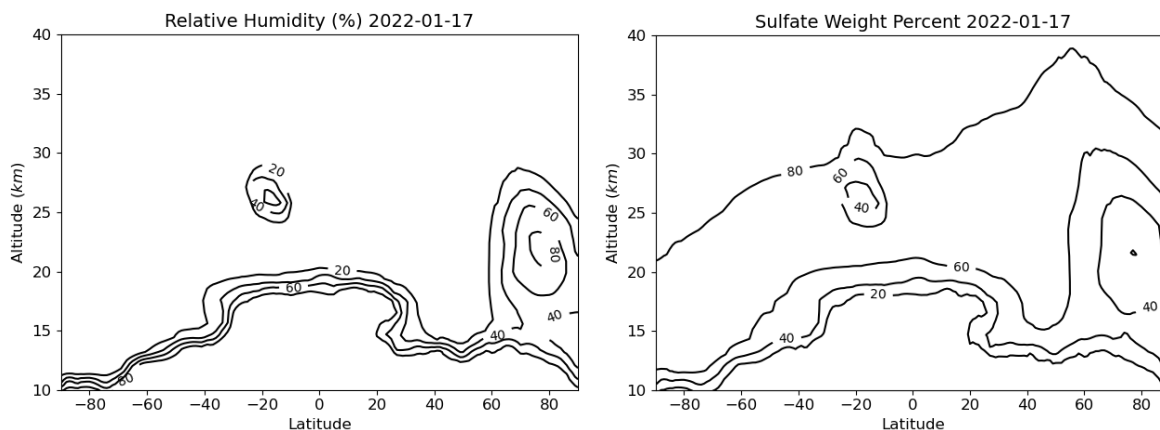
819  
820  
821

Table E1: Comparison of retrieved Hunga AOD and Aerosol Peak Height ( $Z_p$ ) between NOAA-20 OMPS-NP and TROPOMI, for selected along-track OMPS locations from 37 to 42.

along-track (0-based)	NOAA-20 OMPS-NP		TROPOMI (collocated)	
	AOD	$Z_p$ [km]	AOD	$Z_p$ [km]
37	1.30	30.00	1.11	30.24
38	2.42	30.52	2.20	30.43
39	1.36	30.24	1.29	30.31
40	0.86	29.94	0.78	30.32
41	1.35	29.46	0.79	29.96
42	1.35	29.47	1.03	29.68

822 **Appendix F. Simulation of Relative Humidity and Sulfate Weight Percent based on NASA Goddard Earth Observing**  
823 **System Chemistry Climate Model (GEOS CCM)**

824 To quantify the relative humidity and percentage of sulfuric acid (sulfate) by mass in the Hunga aerosol solutions, we used a  
825 version of the GEOS Chemistry Climate Model (GEOS CCM) with the Community Aerosol and Radiation Model for  
826 Atmospheres (CARMA) similar to Case et al. (2023). This version of GEOS CCM: (1) calculates the oxidation of volcanic  
827 sulfur dioxide by online oxidant species and (2) includes a detailed, size-resolved treatment of aerosol microphysics including  
828 diagnosing the amount of water vapor that condenses on hygroscopic aerosols. This model was designed to simulate large  
829 volcanic eruptions and has been validated and used in multiple studies of stratospheric volcanic injections (Case et al., 2023;  
830 Case et al., 2024; Zhu et al., 2025). We initialized this model with 0.5 Tg of SO<sub>2</sub> based on Carn et al. (2022), and consistent  
831 with the results of this study, water vapor such that the model retained about 150 Tg within the plume, as observed by the  
832 Microwave Limb Sounder (MLS). Figure F1 shows a zonal maximum of relative humidity and the associated percentage of  
833 sulfate by mass simulated by the model. In CARMA, the sulfate weight percentage is calculated following the method of  
834 Tabazadeh et al. (1997). Within the Hunga Plume itself, relative humidity values are as high as 60% resulting in a sulfate  
835 weight percent as low as 40%.



836  
837 **Figure F1: (Left) Zonal maximum relative humidity on January 17, 2022 in NASA GEOS CCM CARMA model. (Right) Sulfate**  
838 **(sulfuric acid) weight percentage of total aerosol mass associated with zonal maximum relative humidity.**

839 **Code availability**

840 The VLIDORT RT model and the Mie code used in this work are publicly available free of charge, and can be obtained by  
841 contacting R. Spurr at RT Solutions, Inc. The retrieval package is governed by the GNU Public License Version 3.0 and is  
842 publicly available on Zenodo (<https://doi.org/10.5281/zenodo.17355073>) and on GitHub  
843 (<https://github.com/cwyh3338/Hunga-Tool-Software.git>).

844 **Data availability**

845 TROPOMI data are publicly available from the Sentinels portal (<https://sentinels.copernicus.eu/data-products> ).

846 The reprocessed M2-SCREAM output used in this paper is available upon request from Krzysztof Wargan  
 847 (krzysztof.wargan1@nasa.gov). NASA ground-based AERONET data are available from <https://aeronet.gsfc.nasa.gov/> .

848

849 **Video supplement.** Supplement S1: Spectral Solar Backscattered Ultraviolet (BUV) Radiance Ratios Showing Mid-  
 850 Stratospheric Aerosols from the January 15 2022 Hunga Eruption, as Observed by the Copernicus Sentinel 5 Precursor  
 851 TROPospheric Monitoring Instrument (TROPOMI) on January 17, 2022 (<https://doi.org/10.5446/70186> ),

852 **Author contributions:**

<b>Contributor role</b>	<b>Role definition</b>	<b>HTHH paper authors</b>
<b>Conceptualization</b>	Ideas; formulation or evolution of overarching research goals and aims.	NAK, OT, SC
<b>Data curation</b>	Management activities to annotate (produce metadata), scrub data, and maintain research data (including software code, where it is necessary for interpreting the data itself) for initial use and later reuse.	NG, KW
<b>Formal analysis</b>	Application of statistical, mathematical, computational, or other formal techniques to analyse or synthesize study data.	RS, WC, MC, ESY, OT, SDP, SC, JPV
<b>Funding acquisition</b>	Acquisition of the financial support for the project leading to this publication.	NAK
<b>Investigation</b>	Conducting a research and investigation process, specifically performing the experiments, or data/evidence collection.	NAK, WC, MC, NKr, ESY, DH, TS
<b>Methodology</b>	Development or design of methodology; creation of models.	RS, NK, MC, DL, DH
<b>Project administration</b>	Management and coordination responsibility for the research activity planning and execution.	NAK
<b>Resources</b>	Provision of study materials, reagents, materials, patients, laboratory samples, animals, instrumentation, computing resources, or other analysis tools.	NAK, TS
<b>Software</b>	Programming, software development; designing computer programmes; implementation of the computer code and supporting algorithms; testing of existing code components.	RS, MC, NG, ESY

<b>Contributor role</b>	<b>Role definition</b>	<b>HTHH paper authors</b>
<b>Supervision</b>	Oversight and leadership responsibility for the research activity planning and execution, including mentorship external to the core team.	NAK
<b>Validation</b>	Verification, whether as a part of the activity or separate, of the overall replication/reproducibility of results/experiments and other research outputs.	NAK, NG, AV, SC
<b>Visualization</b>	Preparation, creation, and/or presentation of the published work, specifically visualization/data presentation.	WC, KW, DH
<b>Writing – original draft preparation</b>	Creation and/or presentation of the published work, specifically writing the initial draft (including substantive translation).	DH, NAK
<b>Writing – review &amp; editing</b>	Preparation, creation, and/or presentation of the published work by those from the original research group, specifically critical review, commentary or revision – including pre- or post-publication stages.	RS, NAK, WC, MC, CL, NKr, AV, KW, SC, JPV, PB, TS

853 **Competing interests:**

854 Some authors are members of the AMT editorial board.

855 **Acknowledgements**

856 Support for this work comes through the NASA contract NNG17HP01C. NAK acknowledges additional support from NASA  
857 Earth Sciences Division MEaSUREs program. Won-Ei Choi was supported by an appointment to the NASA Postdoctoral  
858 Program at the Goddard Space Flight Center, administered by Oak Ridge Associated Universities under contract with NASA.  
859 NAK, WC and OT thank Pete Colarco, Parker Case, Mian Chin, Alexander Smirnov, Thomas Eck, and AERONET team for  
860 useful discussions.

861 The KNMI contributions to this work have been funded by the Netherlands Space Office (NSO), as part of the TROPOMI  
862 Science Contract. This publication contains modified Copernicus Sentinel data. Sentinel-5 Precursor is an ESA mission  
863 implemented on behalf of the European Commission. The TROPOMI payload is a joint development by the ESA and the  
864 Netherlands Space Office.

865 The Australian Integrated Marine Observing System (IMOS) and CSIRO are acknowledged for funding the Lucinda  
866 AERONET site. We thank Kahill Mitchell for routine instrument maintenance at the Lucinda site, and David Barker for regular  
867 data transfers to AERONET.

868 **References**

- 869 Asher, E., Todt, M., Rosenlof, K., Thornberry, T., Gao, R.-S., Taha, G., Walter, P., Alvarez, S., Flynn, J., Davis, S. M., Evan,  
870 S., Brioude, J., Metzger, J.-M., Hurst, D. F., Hall, E., and Xiong, K.: Unexpectedly rapid aerosol formation in the Hunga Tonga  
871 plume, *Proc. Nat. Acad. Sci.*, **120**(46), <https://doi.org/10.1073/pnas.2219547120>, 2023.
- 872 Baron, A., Chazette, P., Khaykin, S., Payen, G., Marquestaut, N., Bègue, N., and Dufлот, V: Early Evolution of the  
873 Stratospheric Aerosol Plume Following the 2022 Hunga Tonga-Hunga Ha’apai Eruption: Lidar Observations From Reunion  
874 (21°S, 55°E), *Geophys. Res. Lett.*, **50**(10), <https://doi.org/10.1029/2022GL101751>, 2023.
- 875 Bernath, P., Boone, C., Pastorek, A., Cameron, D., and Lecours, M.: Satellite characterization of global stratospheric sulfate  
876 aerosols released by Tonga volcano, *J. Quant. Spectrosc. Radiat. Transf.*, **299**, 108520.  
877 <https://doi.org/10.1016/j.jqsrt.2023.108520>, 2023.
- 878 Beyer, K. D., Ravishankara, A. R., and Lovejoy, E. R.: Measurements of UV refractive indices and densities of H<sub>2</sub>SO<sub>4</sub>/H<sub>2</sub>O  
879 and H<sub>2</sub>SO<sub>4</sub>/HNO<sub>3</sub>/H<sub>2</sub>O solutions, *J. Geophys. Res.*, **101**(D9), 14519–14524, <https://doi.org/10.1029/96JD00937>, 1996.
- 880 Bian, J., Li, D., Bai, Z., Xu, J., Li, Q., Wang, H., Vömel, H., Wienhold, F. G., and Peter, T.: First detection of aerosols of the  
881 Hunga Tonga eruption in the Northern Hemisphere stratospheric westerlies, *Sci. Bull.*, **68**(6), 574–577.  
882 <https://doi.org/10.1016/j.scib.2023.03.002>, 2023.
- 883 Bhartia, P. K., Herman, J., McPeters, R. D., and Torres, O.: Effect of Mount Pinatubo aerosols on total ozone measurements  
884 from backscatter ultraviolet (BUV) experiments, *J. Geophys. Res. Atmos.*, **98**(D10), 18547-18554.  
885 <https://doi.org/10.1029/93JD01739>, 1993.
- 886 Bodhaine, B., N. Wood, E. Dutton, and J. Slusser: On Rayleigh optical depth calculations. *J. Atmos. Ocean. Tech.*, **20**, 1854-  
887 1861, [https://doi.org/10.1175/1520-0426\(1999\)016%3C1854:ORODC%3E2.0.CO;2](https://doi.org/10.1175/1520-0426(1999)016%3C1854:ORODC%3E2.0.CO;2), 1999.
- 888 Bogumil, K., Orphal, J., Homann, T., Voigt, S., Spietz, P., Fleischmann, O.C., Vogel, A., Hartmann, M., Kromminga, H.,  
889 Bovensmann, H. and Frerick, J.: Measurements of molecular absorption spectra with the SCIAMACHY pre-flight model:  
890 Instrument characterization and reference data for atmospheric remote-sensing in the 230–2380 nm region, in *Atmospheric*  
891 *Photochemistry*, edited by J. P. Burrows and G. K. Moortgat, *J. Photochem. Photobiol.*, **A**, **157**(2–3), 167–184,  
892 [https://doi.org/10.1016/S1010-6030\(03\)00062-5](https://doi.org/10.1016/S1010-6030(03)00062-5), 2003.
- 893 Boichu, M., Grandin, R., Blarel, L., Torres, B., Derimian, Y., Goloub, P., Brogniez, C., Chiapello, I., Dubovik, O., Mathurin,  
894 T., Pascal, N., Patou, M., and Riedi, J.: Growth and Global Persistence of Stratospheric Sulfate Aerosols From the 2022 Hunga  
895 Tonga–Hunga Ha’apai Volcanic Eruption, *J. Geophys. Res. Atmos.*, **128**(23), <https://doi.org/10.1029/2023JD039010>, 2023.
- 896 Bourassa, A. E., Zawada, D. J., Rieger, L. A., Warnock, T. W., Toohey, M., and Degenstein, D. A.: Tomographic Retrievals  
897 of Hunga Tonga-Hunga Ha’apai Volcanic Aerosol. *Geophys. Res. Lett.*, **50**(3), <https://doi.org/10.1029/2022GL101978>, 2023.
- 898 Brion, J., J. Charbonnier, D. Daumont, C. Parisse and J. Malicet: High-resolution laboratory absorption cross section of O<sub>3</sub>  
899 Temperature effect, *Chem. Phys. Lett.*, **213**, 610-612, [https://doi.org/10.1016/0009-2614\(93\)89169-I](https://doi.org/10.1016/0009-2614(93)89169-I), 1993.

900 Bruckert, J., Chopra, S., Siddans, R., Wedler, C., and Hoshyaripour, G. A.: Aerosol dynamic processes in the Hunga plume in  
901 January 2022: does water vapor accelerate aerosol aging? *Atmos. Chem. Phys.*, **25**, 9859–9884, [https://doi.org/10.5194/acp-](https://doi.org/10.5194/acp-25-9859-2025)  
902 25-9859-2025, 2025.

903 Carn, S. A., Krotkov, N. A., Fisher, B. L., and Li, C.: Out of the blue: Volcanic SO<sub>2</sub> emissions during the 2021-2022 eruptions  
904 of Hunga Tonga–Hunga Ha’apai (Tonga), *Front. Earth Sci.*, **10**. <https://doi.org/10.3389/feart.2022.976962>, 2022.

905 Carr, J. L., Horváth, Á., Wu, D. L., and Friberg, M. D.: Stereo Plume Height and Motion Retrievals for the Record-Setting  
906 Hunga Tonga–Hunga Ha’apai Eruption of 15 January 2022, *Geophys. Res. Lett.*, **49**(9),  
907 <https://doi.org/10.1029/2022GL098131>, 2022.

908 Case, P., Colarco, P.R., Toon, B., Aquila, V. and Keller, C.A.: Interactive stratospheric aerosol microphysics-chemistry  
909 simulations of the 1991 Pinatubo volcanic aerosols with newly coupled sectional aerosol and stratosphere-troposphere  
910 chemistry modules in the NASA GEOS Chemistry-Climate Model (CCM). *J. Adv. Model. Earth Syst.*, **15**(8),  
911 <https://doi.org/10.1029/2022MS003147>, 2023.

912 Case, P.A., Colarco, P.R., Toon, O.B. and Newman, P.A.: Simulating the volcanic sulfate aerosols from the 1991  
913 eruption of Cerro Hudson and their impact on the 1991 ozone hole. *Geophys. Res. Lett.*, **51**(5),  
914 <https://doi.org/10.1029/2023GL106619>, 2024.

915 Chong, E.K.P., and Zak, S.H., 2001: An Introduction to Optimization, 2<sup>nd</sup> Ed. Wiley-Interscience, NY, 476 pp. (ISBN 0-471-  
916 39126-3).

917 Dubovik, O. and M. D. King, 2000: A flexible inversion algorithm for retrieval of aerosol optical properties from Sun and sky  
918 radiance measurements, *J. Geophys. Res.*, **105**, 20 673-20 696.

919 Duchamp, C., Legras, B., Podglajen, A., Sellitto, P., Bourassa, A. E., Rozanov, A., Taha, G., and Zawada, D. J.: Aerosol  
920 Composition and Extinction of the 2022 Hunga Plume Using CALIOP. *EGUsphere*, [https://doi.org/10.5194/egusphere-2025-](https://doi.org/10.5194/egusphere-2025-3355)  
921 3355, 2025.

922 Coy, L., Newman, P. A., Wargan, K., Partyka, G., Strahan, S. E., Pawson, S.: Stratospheric circulation changes associated  
923 with the Hunga Tonga–Hunga Ha’apai eruption. *Geophys. Res. Lett.*, **49**(22), <https://doi.org/10.1029/2022GL100982>, 2022.

924 Duchamp, C., Wrana, F., Legras, B., Sellitto, P., Belhadji, R., and Von Savigny, C.: Observation of the Aerosol Plume From  
925 the 2022 Hunga Tonga–Hunga Ha’apai Eruption With SAGE III/ISS, *Geophys. Res. Lett.*, **50**(18),  
926 <https://doi.org/10.1029/2023GL105076>, 2023.

927 Evan, S., Brioude, J., Rosenlof, K. H., Gao, R.-S., Portmann, R. W., Zhu, Y., Volkamer, R., Lee, C. F., Metzger, J.-M., Lamy,  
928 K., Walter, P., Alvarez, S. L., Flynn, J. H., Asher, E., Todt, M., Davis, S. M., Thornberry, T., Vömel, H., Wienhold, F. G., ...  
929 Read, W. G.: Rapid ozone depletion after humidification of the stratosphere by the Hunga Tonga Eruption, *Sci.*, **382**(6668),  
930 <https://doi.org/10.1126/science.adg2551>, 2023.

931 Franz, B. A., Cetinić, I., Ibrahim, A., and Sayer, A. M.: Anomalous trends in global ocean carbon concentrations following  
932 the 2022 eruptions of Hunga Tonga–Hunga Ha’apai, *Commun. Earth Environ.*, **5**(1), 247, [https://doi.org/10.1038/s43247-024-](https://doi.org/10.1038/s43247-024-01421-8)  
933 01421-8, 2024.

934 Gelaro, R., McCarty, W., Suárez, M.J., Todling, R., Molod, A., Takacs, L., Randles, C.A., Darmenov, A., Bosilovich, M.G.,  
935 Reichle, R. and Wargan, K.: The Modern-Era Retrospective analysis for research and applications, version 2 (MERRA-2), *J.*  
936 *Clim.*, **30**(14), 5419–5454, <https://doi.org/10.1175/JCLI-D-16-0758.1>, 2017.

937 Guo, X., and Lu, D.: 2006. Feasibility study for joint retrieval of air density and ozone in the stratosphere and mesosphere with  
938 the limb-scan technique. *Appl. Opt.*, **45**(35), 9021-9030, <https://doi.org/10.1364/AO.45.009021>, 2006.

939 Holben, B.N., Eck, T.F., Slutsker, I.A., Tanre, D., Buis, J.P., Setzer, A., Vermote, E., Reagan, J.A., Kaufman, Y.J., Nakajima,  
940 T. and Lavenu, F.: AERONET—A federated instrument network and data archive for aerosol characterization, *Remote Sens.*  
941 *Environ.*, **66**(1), 1-16, [https://doi.org/10.1016/S0034-4257\(98\)00031-5](https://doi.org/10.1016/S0034-4257(98)00031-5), 1998.

942 Hyman, D. M., and Pavolonis, M. J.: Probabilistic retrieval of volcanic SO<sub>2</sub> layer height and partial column density using the  
943 Cross-track Infrared Sounder (CrIS), *Atmos. Meas. Tech.*, **13**(11), 5891-5921, <https://doi.org/10.5194/amt-13-5891-2020>,  
944 2020.

945 Jaross, G., OMPS-NPP L3 NM Ozone (O3) Total Column 1.0 deg grid daily V2, Greenbelt, MD, USA, Goddard Earth Sciences  
946 Data and Information Services Center (GES DISC), Accessed: December 7, 2025, <https://doi.org/10.5067/7Y7KSA1QNQP8>,  
947 2017.

948 Kelly, L.J., Fauria, K.E., Manga, M., Cronin, S.J., Latu'ila, F.H., Paredes-Mariño, J., Mittal, T. and Bennartz, R.: Airfall  
949 volume of the 15 January 2022 eruption of Hunga volcano estimated from ocean color changes, *Bull. Volcanol.* **86**, 59,  
950 <https://doi.org/10.1007/s00445-024-01744-6>, 2024.

951 Khaykin, S., Podglajen, A., Ploeger, F., Grooß, J.-U., Tence, F., Bekki, S., Khlopenkov, K., Bedka, K., Rieger, L., Baron, A.,  
952 Godin-Beekmann, S., Legras, B., Sellitto, P., Sakai, T., Barnes, J., Uchino, O., Morino, I., Nagai, T., Wing, R., ... Ravetta, F.:  
953 Global perturbation of stratospheric water and aerosol burden by Hunga eruption, *Commun. Earth Environ.*, **3**(1), 316.  
954 <https://doi.org/10.1038/s43247-022-00652-x>, 2022.

955 Kramarova, N. A., et al.: Analysis of anomalies in SNPP OMPS ozone retrievals following the 2022 Hunga eruption,  
956 Quadrennial Ozone Symposium, Boulder, Colorado, US, July 2024,  
957 [https://qos2024.colorado.edu/sites/default/files/2024-07/Group6B\\_Submissions\\_780707\\_2024-06-28.pdf](https://qos2024.colorado.edu/sites/default/files/2024-07/Group6B_Submissions_780707_2024-06-28.pdf), 2024.

958 Kahn, R. A., Limbacher, J. A., Junghenn Noyes, K. T., Flower, V. J., Zamora, L. M., & McKee, K. F.: Evolving particles in  
959 the 2022 Hunga Tonga—Hunga Ha'apai volcano eruption plume, *J. Geophys. Res. Atmos.*, **129**(11),  
960 <https://doi.org/10.1029/2023JD039963>, 2024.

961 Krotkov, N. A., O. Torres, C. Seftor, A. J. Krueger, A. Kostinski, W. I. Rose, G. J. S. Bluth, D. Schneider, and S. J. Schaefer:  
962 Comparison of TOMS and AVHRR volcanic ash retrievals from the August 1992 eruption of Mt. Spurr, *Geophys. Res. Lett.*,  
963 **26**(4), 455–458, <https://doi.org/10.1029/1998GL900278>, 1999a.

964 Krotkov, N.A., D.E. Flittner, A.J. Krueger, A. Kostinski, C. Riley and W. Rose, O. Torres, Effect of particle non-sphericity on  
965 satellite monitoring of drifting volcanic ash clouds, *JQSRT*, **63**, 613-630, [https://doi.org/10.1016/S0022-4073\(99\)00041-2](https://doi.org/10.1016/S0022-4073(99)00041-2) ,  
966 1999b

967 Kubota, T., Saito, T., and Nishida, K.: Global fast-traveling tsunamis driven by atmospheric Lamb waves on the 2022 Tonga  
968 eruption, *Sci.*, **377**(6601), 91-94, <https://doi.org/10.1126/science.abo4364>, 2022.

969 Legras, B., Duchamp, C., Sellitto, P., Podglajen, A., Carboni, E., Siddans, R., Grooß, J.-U., Khaykin, S., and Ploeger, F.: The  
970 evolution and dynamics of the Hunga Tonga–Hunga Ha’apai sulfate aerosol plume in the stratosphere, *Atmos. Chem. Phys.*,  
971 **22**(22), 14957–14970, <https://doi.org/10.5194/acp-22-14957-2022>, 2022.

972 Ludewig, A., Q. Kleipool, R. Bartstra, R. Landzaat, J. Leloux, E. Loots, P. Meijering, E. van der Plas, N. Rozemeijer, F. Vonk,  
973 and P. Veeffkind: In-flight calibration results of the TROPOMI payload on board the Sentinel-5 Precursor satellite, *Atmos.*  
974 *Meas. Tech.*, **13**, 3561–3580, <https://doi.org/10.5194/amt-13-3561-2020>, 2020.

975 Ludewig, A.: S5P Mission Performance Centre Level 1b Readme Report S5P-MPC-KNMI-PRF-L1B, issue 5.0.0, 1 March  
976 2023, KNMI, De Bilt, the Netherlands, available at: [https://sentinel.esa.int/documents/247904/3541451/Sentinel-5P-Level-1b-](https://sentinel.esa.int/documents/247904/3541451/Sentinel-5P-Level-1b-Product-Readme-File)  
977 [Product-Readme-File](https://sentinel.esa.int/documents/247904/3541451/Sentinel-5P-Level-1b-Product-Readme-File), last access: 7 December 2025.

978 Lynett, P., McCann, M., Zhou, Z., Renteria, W., Borrero, J., Greer, D., ... and Cinar, G. E.: Diverse tsunamigenesis triggered  
979 by the Hunga Tonga-Hunga Ha’apai eruption, *Nature*, **609**(7928), 728-733, <https://doi.org/10.1038/s41586-022-05170-6>,  
980 2022.

981 Manney, G. L., Santee, M. L., Lambert, A., Millán, L. F., Minschwaner, K., Werner, F., Lawrence, Z. D., Read, W. G., Livesey,  
982 N. J., and Wang, T.: Siege in the Southern Stratosphere: Hunga Tonga-Hunga Ha’apai Water Vapor Excluded From the 2022  
983 Antarctic Polar Vortex, *Geophys. Res. Lett.*, **50**(14), <https://doi.org/10.1029/2023GL103855>, 2023.

984 Marquardt, D.: An Algorithm for Least-Squares Estimation of Nonlinear Parameters, *J. Soc. Ind. Appl. Math.*, **11**(2), 431–441,  
985 <https://doi.org/10.1137/0111030>, 1963.

986 Matoza, R. S., Fee, D., Assink, J. D., Iezzi, A. M., Green, D. N., Kim, K., ... and Wilson, D. C.: Atmospheric waves and global  
987 seismoacoustic observations of the January 2022 Hunga eruption, Tonga. *Sci.*, **377**(6601), 95-100,  
988 <https://doi.org/10.1126/science.abo7063>, 2022.

989 Mettig, N., Weber, M., Rozanov, A., Arosio, C., Burrows, J. P., Veeffkind, P., Thompson, A. M., Querel, R., Leblanc, T.,  
990 Godin-Beekmann, S., Kivi, R., and Tully, M. B.: Ozone profile retrieval from nadir TROPOMI measurements in the UV range,  
991 *Atmos. Meas. Tech.*, **14**, 6057–6082, <https://doi.org/10.5194/amt-14-6057-2021>, 2021.

992 Millán, L., Santee, M. L., Lambert, A., Livesey, N. J., Werner, F., Schwartz, M. J., Pumphrey, H. C., Manney, G. L., Wang,  
993 Y., Su, H., Wu, L., Read, W. G., and Froidevaux, L.: The Hunga Tonga-Hunga Ha’apai Hydration of the Stratosphere,  
994 *Geophys. Res. Lett.*, **49**(13), <https://doi.org/10.1029/2022GL099381>, 2022.

995 Myhre, C. E., Nielsen, C. J., and Saastad, O. W.: Density and surface tension of aqueous H<sub>2</sub>SO<sub>4</sub> at low temperature, *J. Chem.*  
996 *Eng. Data*, **43**(4), 617-622. <https://www.doi.org/10.1021/je980013g>, 1998.

997 Palmer, K., and D. Williams: Optical Constants of Sulfuric Acid; Application to the Clouds of Venus?, *Appl. Opt.*, **14**, 209-  
998 219, <https://doi.org/10.1364/AO.14.000208>, 1975.

999 Randel, W. J., Johnston, B. R., Braun, J. J., Sokolovskiy, S., Vömel, H., Podglajen, A., and Legras, B.: Stratospheric Water  
1000 Vapor from the Hunga Tonga–Hunga Ha’apai Volcanic Eruption Deduced from COSMIC-2 Radio Occultation, *Remote Sens.*,  
1001 **15**, 2167, <https://doi.org/10.3390/rs15082167>, 2023.

1002 Rodgers, C. D.: *Inverse Methods for Atmospheric Sounding: Theory and Practice*, Series on Atmospheric, Oceanic and  
1003 Planetary Physics, Vol. 2, World scientific, 238 pp., ISBN 981022740X, 2000.

1004 Sadeghi, B., Crawford, A., Chai, T., Cohen, M., Sieglaff, J., Pavolonis, M., ... and Morris, G.: Improving volcanic SO<sub>2</sub> cloud  
1005 modeling through data fusion and trajectory analysis: A case study of the 2022 Hunga Tonga eruption. *J. Geophys. Res.:  
1006 Atmos.*, **130**(4), <https://doi.org/10.1029/2024JD042421>, 2025.

1007 Schoeberl, M. R., and Sparling, L. C.: Trajectory modelling. In Diagnostic tools in atmospheric physics (pp. 289-305). IOS  
1008 Press, 1995

1009 Schoeberl, M. R., Wang, Y., Ueyama, R., Dessler, A., Taha, G., and Yu, W.: The Estimated Climate Impact of the Hunga  
1010 Tonga-Hunga Ha’apai Eruption Plume. *Geophys. Res. Lett.*, **50**(18), <https://doi.org/10.1029/2023GL104634>, 2023.

1011 Sellitto, P., Podglajen, A., Belhadji, R., Boichu, M., Carboni, E., Cuesta, J., Duchamp, C., Kloss, C., Siddans, R., Bègue, N.,  
1012 Blarel, L., Jegou, F., Khaykin, S., Renard, J.-B., and Legras, B.: The unexpected radiative impact of the Hunga Tonga eruption  
1013 of 15th January 2022, *Commun. Earth Environ.*, **3**(1), 288, <https://doi.org/10.1038/s43247-022-00618-z> , 2022.

1014 Sellitto, P., Siddans, R., Belhadji, R., Carboni, E., Legras, B., Podglajen, A., Duchamp, C. and Kerridge, B.: Observing the  
1015 SO<sub>2</sub> and sulfate aerosol plumes from the 2022 Hunga eruption with the Infrared Atmospheric Sounding Interferometer (IASI),  
1016 *Geophys. Res. Lett.*, **51**, <https://doi.org/10.1029/2023GL105565> , 2024.

1017 Shrivastava, M. N., Sunil, A. S., Maurya, A. K., Aguilera, F., Orrego, S., Sunil, P. S., ... and Moreno, M.: Tracking tsunami  
1018 propagation and Island’s collapse after the Hunga Tonga Hunga Ha’apai 2022 volcanic eruption from multi-space  
1019 observations, *Sci. Rep.*, **13**(1), 20109, <https://doi.org/10.1038/s41598-023-46397-1>, 2023.

1020 Sicard, M., Baron, A., Ranaivombola, M., Gantois, D., Millet, T., Sellitto, P., ... and Dufлот, V.: Radiative impact of the Hunga  
1021 stratospheric volcanic plume: role of aerosols and water vapor over Réunion Island (21° S, 55° E), *Atmos. Chem. Phys.*, **25**(1),  
1022 367-381, <https://doi.org/10.5194/acp-25-367-2025>, 2025.

1023 Spurr, R. J. D.: VLIDORT: A linearized pseudo-spherical vector discrete ordinate radiative transfer code for forward model  
1024 and retrieval studies in multilayer multiple scattering media, *J. Quant. Spectrosc. Radiat. Transfer*, **102**(2), 316-342,  
1025 <https://doi.org/10.1016/j.jqsrt.2006.05.005>, 2006.

1026 Spurr, R., J. Wang, J. Zeng, and M. Mishchenko: Linearized T-Matrix and Mie scattering computations, *J. Quant. Spectrosc.  
1027 Radiat. Transfer*, **113**, 425-439, <https://doi.org/10.1016/j.jqsrt.2011.11.014>, 2012.

1028 Spurr, R., and Christi, M.: On the generation of atmospheric property Jacobians from the (V) LIDORT linearized radiative  
1029 transfer models. *J. Quant. Spectrosc. Radiat. Transf.*, **142**, 109-115, 2014.

1030 Spurr, R. and Christi, M.: The LIDORT and VLIDORT linearized scalar and vector discrete ordinate radiative transfer models:  
1031 Updates in the last 10 years, in: Radiative transfer and light scattering (Springer series in light scattering, Volume 3), Springer,  
1032 Berlin, Heidelberg, Germany, 1–62, [https://doi.org/10.1007/978-3-030-03445-0\\_1](https://doi.org/10.1007/978-3-030-03445-0_1), 2019.

1033 Stenchikov, G., Ukhov, A., and Osipov, S.: Modeling the radiative forcing and atmospheric temperature perturbations caused  
1034 by the 2022 Hunga volcano explosion, *J. Geophys. Res. Atmos.*, 130(11), <https://doi.org/10.1029/2024JD041940>, 2025.

1035 Stocker, M., Steiner, A. K., Ladstädter, F., Foelsche, U., and Randel, W. J.: Strong persistent cooling of the stratosphere after  
1036 the Hunga eruption, *Commun. Earth Environ.*, **5**(1), 450, <https://doi.org/10.1038/s43247-024-01620-3>, 2024.

1037 Tabazadeh, A., Toon, O. B., Clegg, S. L., and Hamill, P.: A new parameterization of H<sub>2</sub>SO<sub>4</sub>/H<sub>2</sub>O aerosol composition:  
1038 Atmospheric implications, *Geophys. Res. Lett.*, **24**, 1931–1934, <https://doi.org/10.1029/97GL01879>, 1997.

1039 Taha, G., Loughman, R., Colarco, P. R., Zhu, T., Thomason, L. W., and Jaross, G.: Tracking the 2022 Hunga Tonga-Hunga  
1040 Ha’apai Aerosol Cloud in the Upper and Middle Stratosphere Using Space-Based Observations, *Geophys. Res. Lett.*, **49**(19),  
1041 <https://doi.org/10.1029/2022GL100091>, 2022.

1042 Theys, N., De Smedt, I., Yu, H., Danckaert, T., van Gent, J., Hörmann, C., ... and Van Roozendael, M.: Sulfur dioxide retrievals  
1043 from TROPOMI onboard Sentinel-5 Precursor: algorithm theoretical basis, *Atmos. Meas. Tech.*, **10**(1), 119-153,  
1044 <https://doi.org/10.5194/amt-10-119-2017>, 2017.

1045 Toon, O.B. and Pollack, J.B.: Physical properties of the Stratospheric aerosols, *J. of Geophys. Res.*, vol. 78, NO. 30, 1973.

1046 Torres, O. and Bhartia, P. K.: Effect of stratospheric aerosol on ozone profile from BUW measurements, *Geophys. Res. Lett.*,  
1047 **22**, N3, <https://doi.org/10.1029/94GL02994>, 1995.

1048 Veeffkind, J. P., Aben, I., McMullan, K., Förster, H., de Vries, J., Otter, G., Claas, J., Eskes, H. J., de Haan, J. F., Kleipool, Q.,  
1049 van Weele, M., Hasekamp, O., Hoogeveen, R., Landgraf, J., Snel, R., Tol, P., Ingmann, P., Voors, R., Kruizinga, B., ... Levelt,  
1050 P. F.: TROPOMI on the ESA Sentinel-5 Precursor: A GMES mission for global observations of the atmospheric composition  
1051 for climate, air quality and ozone layer applications, *Remote Sens. Environ.*, **120**, 70–83,  
1052 <https://doi.org/10.1016/j.rse.2011.09.027>, 2012.

1053 Vömel, H., S. .Evan, and M. Tully: Water vapor injection into the stratosphere by Hunga Tonga-Hunga Ha’apa, *Sci.*, **377**,  
1054 1444-1447, <https://doi.org/10.1126/science.abq2299>, 2022.

1055 Wargan, K., Weir, B., Manney, G. L., Cohn, S. E., Knowland, K. E., Wales, P. A., and Livesey, N. J.: M2-SCREAM: A  
1056 stratospheric composition reanalysis of Aura MLS data with MERRA-2 transport, *Earth Space Sci.*, **10**,  
1057 <https://doi.org/10.1029/2022EA002632>, 2023.

1058 Zhu, Y., Bardeen, C. G., Tilmes, S., Mills, M. J., Wang, X., Harvey, V. L., Taha, G., Kinnison, D., Portmann, R. W., Yu, P.,  
1059 Rosenlof, K. H., Avery, M., Kloss, C., Li, C., Glanville, A. S., Millán, L., Deshler, T., Krotkov, N., and Toon, O. B.:  
1060 Perturbations in stratospheric aerosol evolution due to the water-rich plume of the 2022 Hunga-Tonga eruption, *Commun.*  
1061 *Earth Environ.*, **3**, 248, <https://doi.org/10.1038/s43247-022-00580-w>, 2022.

1062 Zhu, Y., Portmann, R. W., Kinnison, D., Toon, O. B., Millán, L., Zhang, J., Vömel, H., Tilmes, S., Bardeen, C. G., Wang, X.,  
1063 Evan, S., Randel, W. J., and Rosenlof, K. H.: Stratospheric ozone depletion inside the volcanic plume shortly after the 2022  
1064 Hunga Tonga eruption, *Atmos. Chem. Phys.*, **23**(20), 13355–13367, <https://doi.org/10.5194/acp-23-13355-2023>, 2023.

1065 Zhu, Y., Akiyoshi, H., Aquila, V., Asher, E., Bednarz, E.M., Bekki, S., Brühl, C., Butler, A.H., Case, P., Chabrillat, S. and  
1066 Chiodo, G., Hunga Tonga–Hunga Ha’apai Volcano Impact Model Observation Comparison (HTHH-MOC) project:

1067 experiment protocol and model descriptions. *Geosci. Model Dev.*, **18**(17), <https://doi.org/10.5194/gmd-18-5487-2025>  
1068 , 2025.